7-2019

Evaluation of VIIRS Nightfire Product and Comparison with MODIS and VIIRS Active Fire Products in a Russian Gas Flaring Region.

Ambrish Sharma
University of Nebraska - Lincoln, ambrish.sharma@huskers.unl.edu

EVALUATION OF VIIRS NIGHTFIRE PRODUCT AND COMPARISON WITH MODIS AND VIIRS ACTIVE FIRE PRODUCTS IN A RUSSIAN GAS FLARING REGION

By

Ambrish Sharma

A THESIS

Presented to the Faculty of

The Graduate College at the University of Nebraska

In Partial Fulfilment of Requirements

For the Degree of Master of Science

Major: Earth and Atmospheric Sciences

Under the Supervision of Professor Mark R. Anderson

Lincoln, Nebraska

July, 2019

EVALUATION OF VIIRS NIGHTFIRE PRODUCT AND COMPARISON WITH MODIS AND VIIRS ACTIVE FIRE PRODUCTS IN A RUSSIAN GAS FLARING REGION

Ambrish Sharma, M.S.

University of Nebraska, 2019

Advisor: Mark R. Anderson

Gas flaring is a commonly used practice for disposing of waste gases emerging from industrial oil drilling and production processes. It is a serious environmental and economic hazard with adverse impacts on air quality, climate, and the public health. Accurate determination of flare locations and estimation of associated emissions are therefore of prime importance. Recently developed Visible Infrared Imaging Radiometer Suite (VIIRS) Nightfire product (VNF) has shown remarkable efficiency in detecting gas flares globally, owing primarily to its use of Shortwave Infrared (SWIR) band in its detection algorithm. This study compares and contrast nocturnal hot source detection by VNF to detections by other established fire detection products (i.e., Moderate Resolution Imaging Spectroradiometer (MODIS) Terra Thermal Anomalies product (MOD14), MODIS Aqua Thermal Anomalies product (MYD14) and VIIRS Applications Related Active Fire Product (VAFP)) over an extensive gas flaring region in Russia - Khanty Mansiysk Autonomous Okrug, for the time period of April - August 2013. The surface hotspots detected by VNF were found to be much higher in magnitude than detected by other products. An attempt to replicate VNF algorithm locally for better comprehension, revealed threshold related discrepancies in VNF V1.0 in multiple spectral bands. Case studies for reconciliation between VNF-R (VNF replicated product) and VAFP hotspots

showed that convergence in hotspot detection between two products is possible by scaling up VNF-R thresholds, and, VAFP can detect large flares having strong spectral signature in SWIR bands. The efficacy of VNF hotspot detection was evaluated for 10 previously identified flare locations with varying hot source sizes over the period of April-August 2013. VNF was able to detect all the test sites with frequency of detection varying between 20% to 42% of the days tested. Mean areas of tested gas flares estimated by VNF showed good agreement with areas of flares computed using Google Earth with a linear correlation of 0.91; however, VNF estimated areas were found to be somewhat underestimated. Overall the results indicate significant potential of VNF in characterizing gas flaring from space.

ACKNOWLEDGEMENT

I am immensely grateful to Prof. Mark R. Anderson, my academic advisor, for his invaluable contribution towards revision and improvement of this work. His insights, critiques and suggestions were indispensable to the upgradation and completion of this thesis. I extend my gratitude to Prof. Clinton Rowe and Prof. Steve Hu for serving on my examination committee and participating meticulously in the review process. I am also thankful to my former advisor Prof. Jun Wang for giving me the opportunity of this research work and guiding me through it. Former committee member Prof. Robert Oglesby also contributed to the clarity and direction of this research. I acknowledge the support provided by the Department of Earth and Atmospheric Sciences, UNL and Holland Computing Centre, UNL for aiding and facilitating my research work. Finally, I am most thankful to my family for their sacrifices, unconditional love and firm belief in me. I must also thank former colleagues for their assistance and Dr. Deepali Rathore without whose support this completion would not be possible.

Table of Contents

List of Figures

List of Tables

1. Introduction

Gas flaring is a global environmental hazard severely impacting air quality, economy, climate, vegetation and public health (Ismail and Umukoro 2012). According to World Bank estimates, over 140 bcm (billion cubic meters) of natural gas is being flared or vented globally each year, which adds about 350 million tons of carbon dioxide to the atmosphere in addition to other harmful impacts (World Bank 2018). Flaring is a high-temperature oxidation process used to burn combustible components, mostly constituting hydrocarbons of waste gases from industrial operations (Gervet 2007). Flaring is widely used to dispose of economically unprofitable waste gases emerging with oil, in addition to acting as a safety device for preventing overpressuring of vessels, however, because of lack of developed infrastructure flaring at large number of sites results in wastage of valuable energy resources. Profuse amounts of world's energy supply are continuously lost through the flaring of gas, contributing to the global carbon emission budget (Casadio et al. 2012b). Apart from greenhouse gases like methane and carbon dioxide and pollutants like, nitrogen dioxide (NO_2), sulphur dioxide (SO_2) and carbon monoxide (CO), the flares contain widely-recognised toxins, such as benzene (C_6H_6), benzopyrene ($C_{20}H_{12}$), carbon disulphide (CS_2), carbonyl sulphide (COS) along with harmful metals such as mercury, arsenic and chromium (Friends of the Earth International 2005). Gas flare emissions pose a great threat to human health, built up environmental and social well-being of inhabitants from host communities (Nwanya 2011). Thus, it becomes pertinent to characterize gas flaring activity and its associated emissions, both spatially and temporally.

1.1 Background

The earliest detection of gas flaring using satellite remote sensing dates back to the early 1970s, when Croft (1973) observed nighttime imagery (mainly over Africa) using a low-light sensor (operating in spectral range of 0.4-1.1 μm) belonging to the United States Air Force Data Acquisition and Processing Program (DAPP) [DAPP system is now called Defense Meteorological Satellite Program (DMSP)], and found gas flares to be the brightest features observed in the visible band. Croft (1978) used the imagery from the DAPP sensor along with Landsat Multi-spectral Scanner System to observe gas flares in many parts of the world including Algeria, Libya, Nigeria, the Persian Gulf, Siberia and Mexico. Croft (1978) used visual identification and manual analysis procedures for the identification of flares from the images and reasserted that the gas flares associated with world's major oil fields were the brightest human-made features observed from space. Further, Muirhead and Cracknell (1984) used the daytime imagery from NOAA's Advanced Very High Resolution Radiometer (AVHRR) to detect offshore gas flaring sites in the North Sea. Their detections were based on the low brightness values observed during daytime in the infrared channel (3.55 μm - 3.93 μm) of AVHRR, from the pixels containing gas flares. Much later, the DMSP Operational Linescan System (OLS) products were used to produce maps of gas flares, fishing boats, fires and human settlements for 200 nations (Elvidge et al. 2001) as a part of a first study to detect gas flaring globally. Further analyses of DMSP-OLS products provided the first record of long-term (1994-2005) gas-flaring volumes (Elvidge et al. 2007) through an ad-hoc calibration method. Later, these flaring

and emission estimate products were extended to 2008 (Elvidge et al. 2009). Although these studies were able to characterize some gas flaring sites, their procedure relied on visual inspection of images (circularity and bright centers of flares), which was not time efficient. Also the spatial resolution of the instruments (e.g., smoothed nominal spatial resolution of 2.7 km for DMSP-OLS) wasn't usually high enough to resolve accurately the flare location, particularly if the flares were situated in proximity of bright urban areas.

The first study that objectively identified hot sources such as flares was done by Matson and Dozier (1981) who found that gas flares could be identified using hot source signals in mid-wave infrared (MWIR) at approximately the 3.7 μm wavelength channel and the 11 μm longwave infrared (LWIR) channel from AVHRR's nighttime imagery, for determining surface temperatures of sub-pixel fires. The method highlighted pixels with combustion sources based on the brightness temperature difference between MWIR and LWIR channels. This formed the basis of fire detection algorithms for many sensors (e.g. Moderate Resolution Imaging Spectroradiometer (MODIS), AVHRR, Visible Infrared Imaging Radiometer Suite (VIIRS) in years to come (Giglio et al. 2003; Weaver et al. 2004; Csiszar et al. 2014). These fire products were designed to detect wildfires and biomass burning; however, they lacked sensitivity to gas flare detections, as gas flares burn at much higher temperatures. Much later, an active flare detection algorithm for global flare monitoring was developed by Casadio et al. (2012b) using Along Track Scanning Radiometers (ATSR) short-wave infrared (SWIR) band imagery, which had previously been exploited for volcanic activity monitoring (Rothery et al. 2001). Their fixed threshold algorithm, based on SWIR radiance values, offered significant improvement in detecting hotspots over previous manual detection methods, although the low spatial resolution of

the ATSR instrument (1000 m at NADIR) still posed a limitation on the accuracy of flare detection, especially when more accurate estimations of flare locations and flaring volumes are desired (Anejionu et al. 2015). Casadio et al. (2012a) further revised their algorithm by an integrated use of ATSR and Synthetic Aperture Radar (SAR) nighttime products for detecting flares in the North Sea.

More recently, Elvidge et al. (2013) have developed an algorithm using SWIR bands (1.6 µm channel as primary detection band) data from high resolution VIIRS nighttime imagery for global fire activity monitoring, called VIIRS Nightfire (referred to as VNF product hereafter in this study). The VNF algorithm also uses five other spectral bands in the near infrared, medium wave infrared region and a panchromatic Day-Night band (DNB) for additional quality checks on detections.

Anejionu et al. (2014) also developed an objective flare detection method based on multispectral infrared band data from Landsat imagery (having high spatial resolution of 30 m). The detections were nonetheless confined to Niger data only and their method was handicapped by limitations such as low frequency of available cloud-free images and unavailability of nighttime Landsat data. Anejionu et al. (2015) recently used MODIS data to develop a revised flare detection and flare volume estimation technique over Nigeria, because of the higher temporal resolution of the MODIS instrument and the availability of nighttime multi-spectral data. However, the drawbacks of using MODIS data are: 1) the lower spatial resolution (1km at nadir) as compared to Landsat and 2) the SWIR MODIS bands [band 6 (1.628-1.652 µm) and band 7 (2.105 -2.155 µm) that are more sensitive to flare detections] are turned off during nightmode scans (Ahmad et al. 2002), so they had to rely on MWIR bands (21-22, both centred on 3.96 µm, however differing in spectral

radiance and noise equivalent temperature difference sensitivity), used mainly for detecting biomass burning. Nevertheless, all these efforts have paved the way for more precise and automated detections of gas flares globally, and so moving forward, a comprehensive study of new active gas flaring products would be beneficial in this direction.

1.2 About this study

Despite the availability of high resolution data from new generation satellite sensors, there have been only a limited number of studies to monitor gas flaring from space and the products are not well-validated (Casadio et al. 2012b; Anejionu et al. 2015). Therefore, a detailed analysis of performance of nighttime fire products over gas flaring regions is necessary.

The objective of this work is to evaluate the efficiency of using data from multiple satellite sensors to assess gas flaring activity from space over an extensive gas flaring region. The test region used for the study is Khanty Mansiysk Autonomous Okrug, Russia. The choice of the region is based on the fact that Russia has emerged as the biggest flaring region of the world lately (Elvidge et al. 2009) and the satellite-based estimate of gas flaring volumes reported from Khanty Mansiysk region alone account for almost 50% of total Russian flaring (Elvidge et al. 2007; Casadio et al. 2012b). Russia is believed to be responsible for a quarter to a third of global associated gas flaring. Recent World Bank report using data from NOAA shows Russia flares about 35 bcm of gas per year and the related economic losses account for $5 billion per year (World Bank 2013). However, domestic assessments claim only about 15-20 bcm of gas is flared annually in Russia. These discrepancies are due to the lack of sufficient instrumentation required to generate

precise statistics on flaring volumes (Oil and Gas Eurasia 2009). According to the Government of Khanty Mansiysk Autonomous District, only half of the flare units operating were equipped with metering devices as of 2007, which worsens the problems for estimation of flaring volumes, required to assess added burden on global carbon budget (Knizhnikov and Poussenkova 2009). In view of these inconsistencies and the need to monitor gas flaring activity efficiently, it is highly important to study the large gas flaring regions in Russia such as Khanty Mansisyk using more effective and reliable methods. In contrast to the ground-based observations, satellite remote sensing provides remarkable spatial (and sometimes temporal) advantages because of the routine and global coverage by the satellite sensors.

This study primarily assesses the performance of the existing fire products quantitatively over the test region. It is well known that factors such as differences in sensor characteristics, spatial resolution and along-scan aggregation schemes play an important role in resultant fire detections differences (even when the satellites on which the sensors are aboard have similar orbital characteristics, as in the case of VIIRS on board Suomi National Polar-orbiting Partnership (NPP) & MODIS on board Aqua). This study investigates other important factors as well, such as the choice of a primary detection band, which determines the efficiency of hot source detections during nighttime. This work also looks into the working of newly developed (and seemingly more efficient, however, not well validated) VNF algorithm and reports some inconsistencies in the version 1.0 of the product. Additionally, this study attempts to reconcile the detection differences between VNF and other fire products, evaluate the performance VNF products on known flaring sites and perform validation of some key parameters reported by the VNF.

Chapter 2 provides details about the datasets used in this study and the study region. Chapter 3 and Chapter 4 describe the methodologies and results respectively. Chapter 5 presents conclusions of the study and, finally, Chapter 6 presents some important updates occurring between the completion of research and publication of this thesis.

2. Data & Region of Study

2.1 Data

Four different fire detection products based on satellite sensor data were used in this study to monitor gas flaring activity over the study region. The four products are: NASA's MODIS fire products, MOD14 and MYD14; NOAA's VIIRS Active Fires Applications Related Product, (called VAFP in this study); and NOAA's VIIRS Nightfire (referred to as VNF in this study) product. Nighttime data from all four products were acquired for five summer months (April - August) of 2013. The following subsections describe the datasets used in this study.

2.1.1 MODIS Fire Products (MOD14 and MYD14)

The MOD14 and MYD14 are the level-2 Fire and Thermal Anomalies products derived from the radiances observed in the MWIR and LWIR channels of MODIS instruments residing on NASA Earth Observing System (EOS) Terra and EOS Aqua satellites respectively. Both Aqua and Terra acquire data twice a day (once each in nighttime and daytime) about three hours apart from each other and are used to produce level-2 swath data at 1 km resolution on a daily basis. The detection algorithm is based on the brightness temperatures derived from MODIS 4 μm and 11 μm channels (Justice et al. 2002; Giglio et al. 2003). The detection function on either an absolute test, where the derived brightness temperature of the potential fire pixel is more than the predetermined threshold, qualifying it as a fire containing pixel, or a contextual test, where a series of tests are employed to detect fire pixels having a temperature difference with the background large enough so as to be qualified as a fire pixel. Apart from

providing the geolocation of the fire detected, the science data sets in the product provide information on fire mask, fire radiative power and quality flags for the algorithm. For this study, MODIS Collection 5 Fire and Thermal Anomalies products, MOD14 and MYD14, were downloaded from NASA's Lands Processes Distributed Active Archive Center (LPDAAC 2014).

2.1.2 VIIRS Active fire product (VAFP)

The VIIRS VAFP is the fire detection product derived from radiances obtained in MWIR and LWIR channels of VIIRS instrument aboard Suomi National Polar-Orbiting Partnership (NPP), launched in October 2011. The EOS MODIS Collection 4 Fire and Thermal Anomalies Algorithm (Giglio et al. 2003) forms the basis of the algorithm for this product (Csizar et. al 2014). The tests used to identify fire-containing pixels in VAFP product are similar to the ones used in the MODIS fire detection algorithm. The primary channels used for this algorithm are M13 (3.9 - 4.1 μm) and M15 (10.2 -11.2 μm) bands. Although the spectral placement of these channels is a little different from MODIS, the same basic algorithm is applicable to these channels. VIIRS on board Suomi NPP has a similar overpass time as MODIS on board Aqua but they differ in spatial resolution (VIIRS having higher spatial resolution than MODIS) and along-scanline aggregation schemes, so the difference in detection between these products stems mostly from these reasons. At present the VAFP only reports the geolocation of pixels detected as containing hot sources. VAFP data for this study were downloaded from NOAA's Comprehensive Large Array Data Stewardship System (CLASS 2014).

2.1.3 NOAA's VIIRS Nightfire product (VNF)

The Nightfire product, VNF, developed by Elvidge et al. (2013), provides daily nocturnal fire monitoring data globally. The product operates on level-2 Sensor Data Records (SDR) data from VIIRS sensor aboard Suomi NPP. It uses radiances observed in visible, near-infrared (NIR), SWIR, MWIR and DNB spectra, which is primarily based on detections in SWIR band (1.6 μm) that corresponds to the M10 band in VIIRS. The SWIR bands prove advantageous for hot source detection during nighttime as high radiant emissions from the hot sources recorded by them stand out in contrast to the sensor noise recorded otherwise. The product provides crucial parameters such as subpixel fire area, radiant heat, radiant heat intensity and fire temperature based on Planck curve fitting, along with the geolocation and other metadata such as radiance thresholds, quality flags and cloud mask. VNF version 1.0 data for this study were downloaded from NOAA's National Geophysical Data Center (NGDC 2014).

Preliminary testing of nighttime detections by the four aforementioned fire products during the period May-July 2013, demonstrates that gas flares are quite abundant in the study region (Fig. 2.1), the VNF product is apparently able to detect them more efficiently than other products, as it explicitly utilizes the shortwave bands to detect hot sources, like flares, even with small surface areas on the order of only a few square meters. The cumulative impact on the number of detections is much larger when we observe detections over a larger area for a couple of months.

2.2 Study Region

The Khanty Mansisyk Autonomous Okrug region chosen for this study has a moderate continental climate. The winters are very long, snowy and cold (temperatures can reach -30 °C in winters), and, the summers are short and warm. A characteristic feature of the climate of this region is rapid changes of weather in spring and summer, and significant daily temperature drops (ADMHMAO, 2019). The average January precipitation is 25 mm and the average July precipitation is 59 mm, whereas, the average January temperature is -22.6 °C and the average July temperature is 18.1 °C (Federation Council, 2019).

For this study, MOD14, MYD14, VAFP and VNF products were used over a 10° x 10° region (55° N - 65° N, 65° E -75° E) which covers areas from the region of interest Khanty Mansiysk Autonomous Okrug in Russia and some neighboring states such as, Yamalia and Tyumen Oblast (Fig. 2.2).

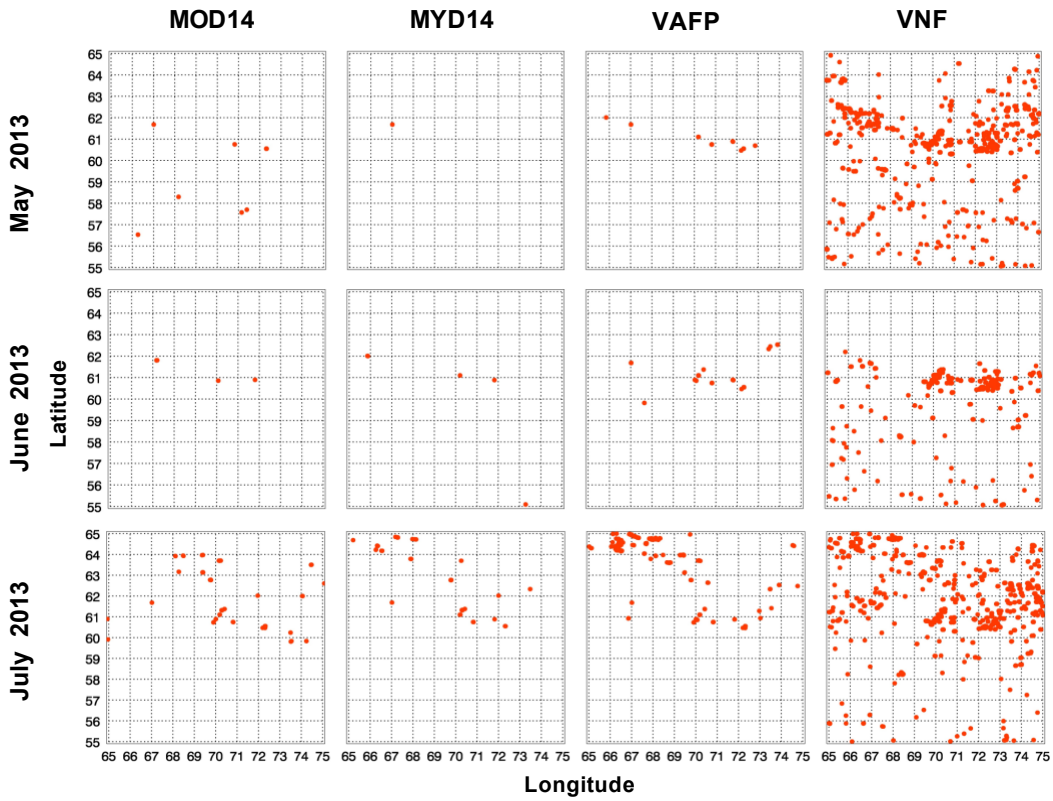

Figure 2.1 Nighttime fire detections by MOD14, MYD14, VAFP and VNF over the study area during summer 2013.

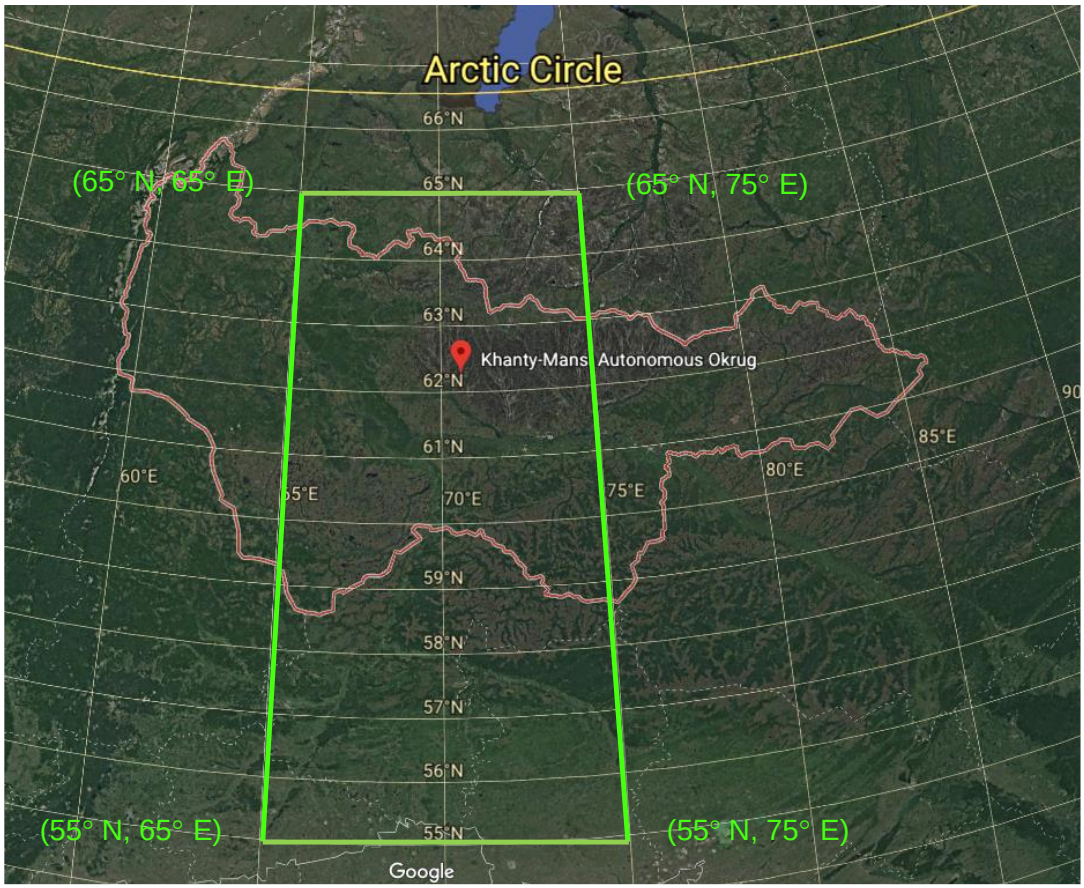

Figure 2.2 Test region (highlighted in green) covering parts of Khanty Mansiysk Autonomous Okrug (red boundaries), Russia. Image Courtesy: Google Earth.

3. Methods

This chapter is divided into five sections, with each section detailing the methodology for a distinct objective. The following sections describe methods used for creating the gas flaring map using VNF data, replication of the VNF algorithm (creating the replicated product, VNF-R), reconciliation between VAFP and VNF-R, temperature and fire area sensitivity analysis, and evaluation of the VNF product, respectively.

3.1 The gas flaring map and hotspot detection by multiple products

Preliminary analyses indicated that the VNF product detected a greater amount of nocturnal fire activity in the study area than any of the other products (Fig. 2.1). Therefore, the VNF product was used to produce a baseline map that would demarcate the gas flaring regions within the study area. This demarcation of flaring regions was done to quantify the number of detections made by different fire products within and outside the highlighted gas flaring regions, in order to evaluate the fire product performance. The entire study area was broken down into an array of $0.25° \times 0.25°$ grid cells. Persistence of detection within the cells and associated high temperature were used as the criteria for delineating the gas flaring regions. The hotspots detected by the VNF were collocated over the reference grid for each day (a total of 153 days were used). Only the detections having cloud mask as clear and having temperatures higher than 1600 K (temperature criterion from Elvidge et. al 2013) were used and marked as valid, the rest of the detections were removed. The total number of valid detections within each cell were recorded for each day. For each cell, a frequency counter was set up to count the number of days when clear-sky, hot spot activity was observed. Finally,

the cells having at least 15 days (almost 10% of total days studied) of hotspot activity were highlighted as gas flaring regions.

Once the gas flaring regions were determined, detections from MOD14, MYD15, VAFP and VNF falling within and outside of these demarcated gas flaring regions for five months (April to August) of 2013 were recorded. In addition, detection counts for each cells from the VNF product were divided into two categories based on associated brightness temperatures (T_B), a) $T_B < 1600K$ and b) ($T_B \geq 1600K$), to see how detections from both these temperature ranges align with the gas flaring regions, with the latter range representing hotter sources (temperatures characteristic of flares). The separation by T_B is also helpful in the characterization of the hot source type (gas flares or forest fires, biomass burning etc.) found in the study area along with spatial pattern of their occurrence. The gas flaring regions determined using VNF product along with nighttime detections from MOD14, MYD14 and VAFP products for five months (March to August) of 2013 are shown in Section 4.1.

3.2 The VNF algorithm and its replication

The observed higher detection counts from the VNF product in the study area motivated the need to understand the functioning of the VNF product better. The first part of this section present briefly to the readers the theoretical basis of the VNF algorithm and second part describes the VNF algorithm flow and compares it to MODIS fire product algorithm respectively. The third part of this section deals with the replication of VNF algorithm as performed (to the extent possible) on our local machines to comprehend VNF's operation in greater detail. It discusses the procedures undertaken to replicate VNF locally and create the replicated product, VNF-R.

3.2.1 The VNF algorithm theoretical background

The VNF detection algorithm is a hotspot identification algorithm that detects and characterizes subpixel hot sources using nocturnal data from various VIIRS spectral bands.

The hot source detection from space-borne instruments is based on Planck's law which states that the characteristic radiation emitted by a blackbody is dependent on its absolute temperature.

$$R(\lambda,T) = \frac{2hc^2}{\lambda^5}\frac{1}{e^{(hc/(\lambda K_B T))}-1} \quad (1)$$

where R is the spectral radiance ($W.sr^{-1}.m^{-2}.\mu m^{-1}$), T is the absolute temperature (K), λ is the wavelength (μm), h is the Planck constant ($6.62 \times 10^{-34}\ m^2.kg.s^{-1}$), K_B is the Boltzmann constant ($1.38 \times 10^{-23}\ m^2.kg.s^{-2}.K^{-1}$), c is the speed of light ($3.0 \times 10^8\ m.s^{-1}$). Planck's law provides the basis for another important law used in fire detection, i.e., Wien's displacement law, which states that the warmer the object, the shorter the wavelength of its peak radiant emission.

$$\lambda_{max} = C_w/T \quad (2)$$

where C_w is Wien's constant (2.89×10^{-3} m.K), T is the temperature of the object (K), λ_{max} is the wavelength of peak emitted radiation (μm).

The peak radiation emitted from a typical flaming fire surface (temperature ~1000 K) lies mostly near the MWIR region of the electromagnetic spectrum. However, gas flares burn at very high temperatures (~1600 K and above) and thus their peak radiant emissions are at much shorter wavelengths, i.e. in SWIR. Planck function curves are shown in Fig. 3.1, to demonstrate how peak radiance shifts to shorter wavelengths for hotter sources. VIIRS has a unique collection of SWIR and near-IR bands that are used as imaging bands during the daytime and record sensor noise during nighttime with an exceptional ability to detect hot sources (Zhizhin et al. 2013). The VNF algorithm essentially exploits these bands, primarily the M10 band (centered on 1.6 μm) for hot source detection. The other spectral bands used by VNF are M7, M8, M12, M13 and DNB (Table 3.1).

A special property of VIIRS data are that the increase in M-Band pixel size from nadir to the edge of the scan is constrained by a varying on-board pixel aggregation scheme (Cao et al. 2014). From nadir up to scan angle < 31.72°, signals from three pixels are aggregated together (zone 3:1), from 31.72° up to scan angles < 41.86°, signals from two pixels are aggregated (zone 2:1) and then from 41.86° up to scan angles 56.28°, no aggregation is done (zone 1:1). For detections in M10, M7 and M8 bands, the VNF calculates separate sets of thresholds for these three aggregation zones by grouping pixels of same aggregation zone together. This is done to make detections as sensitive as possible in these bands since the aggregation scheme alters the signal to noise ratio in these aggregation zones, as it constrains the pixel size (Elvidge et al.

2013). Fig. 3.2 helps in better visualization of these aggregation zones in the VIIRS swath

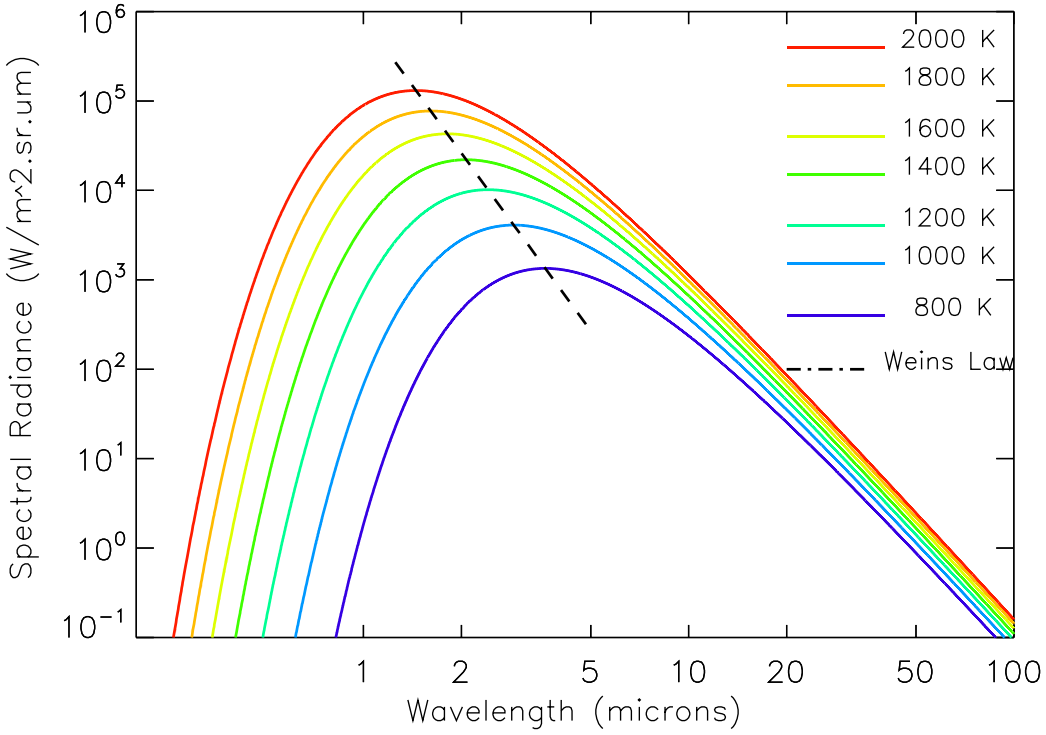

Figure 3.1 Blackbody spectrum for different temperature sources.

Table 3.1 Suomi-NPP VIIRS channels used in the VNF algorithm.

VIIRS band name	Central wavelength (µm)	Bandwidth (µm)	Wavelength range (µm)	Band Type
M7	0.865	0.039	0.846-0.885	Near IR
M8	1.240	0.020	1.230-1.250	Near IR
M10	1.610	0.060	1.580-1.640	Short Wave IR
M12	3.700	0.180	3.610-3.790	Med. Wave IR
M13	4.050	0.155	3.970-4.130	Med. Wave IR
DNB	0.700	0.400	0.500-0.900	Panchromatic

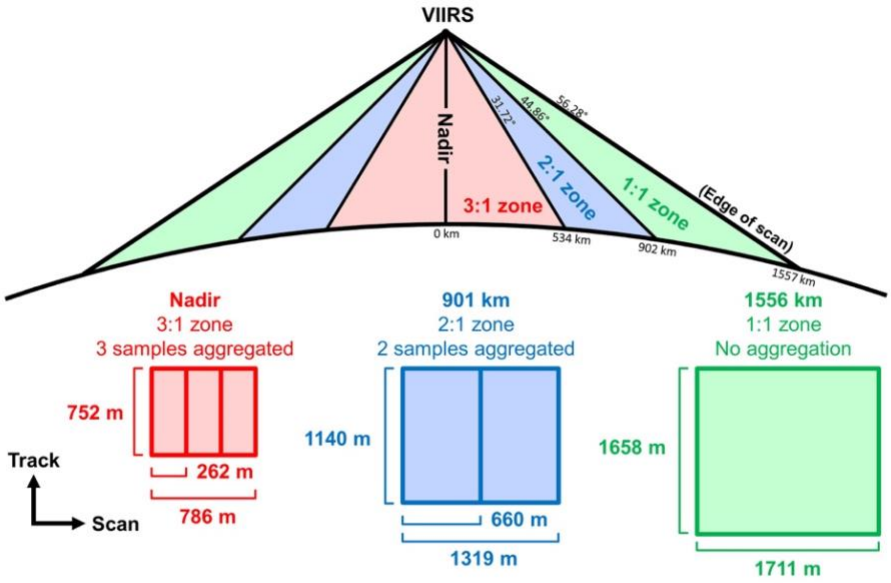

Figure 3.2 Aggregation zones in VIIRS swath. Source: (Polivka et al. 2015)

3.2.2 VNF and MODIS fire detection algorithms

The VNF is an M10 band based algorithm, thus the candidate hot pixels are chosen on the basis of anomalously high values in the M10 band (Fig 3.3) All the pixels are first prescreened for solar contamination; to eliminate the solar glint, only pixels with solar zenith angles (SZA) greater than 95° are approved. The approved pixels are then pooled together according to their aggregation zones. Background statistics mean (μ) and standard deviation (δ) are calculated using M10 digital numbers (DN), unsigned integers recorded in VIIRS sensor data record files which can be converted to radiances using scale factor and offset values. Pixels with DN greater than 100 are excluded from background calculations to remove any bias caused by obviously hot pixels in threshold calculations. For each aggregation zone a threshold of ($\mu + 4\times \delta$) is set and pixels having M10 DN higher than the threshold of their respective zone are designated as candidate hot pixels.

Next, the VNF algorithm searches if these candidate pixels are hot in other bands as well. Corresponding pixels are located in M7 and M8 bands using line and sample numbers of M10 hot pixels. The background statistics are calculated for thresholds (calculated in radiance instead of DN) in M7 and M8 bands in the same manner as in M10. If the corresponding pixels have radiance values above the thresholds calculated for M7 and M8 bands, then the pixels are marked as hot in these bands.

For M12 and M13 (both MWIR bands) the threshold calculation is different than SWIR bands as earth surface and cloud features complicates the analysis for them. The thresholds are calculated using a 10×10 window around the pixel corresponding to a M10 hot pixel. Any pixels corresponding to other hot M10 pixels found within the 10×10 window, are excluded from the 10×10 window background statistics calculations; that is, the mean and standard deviation for threshold calculation are calculated using the rest of pixels in the background. If fewer than 50 background pixels are found within the 10×10 window, the window is expanded to 100×100. The hot pixel threshold in M12 and M13 is set as ($\mu + 3\times \delta$). Candidate pixels (pixel in M12 and M13 corresponding to M10 hot pixel) exceeding this threshold are marked as hot in these bands.

The VNF algorithm then uses line and scan angle to approximate a DNB location corresponding to an M10 hot pixel that is also local maxima (pixels where immediate neighbours have low DN values) in M10. Exact spatial matches are not possible because of different pixel width in DNB pixels in correspondence to M10 hotspots. If DNB local maxima are identified, metadata (DNB radiance, geolocation, quality flag etc.) for that pixel are recorded.

The VNF algorithm then moves to noise filtering, atmospheric filtering, Planck curve fitting (for sub-pixel fire area and temperature calculations) and cloud cover analysis parts; however, the scope of this study is confined to hotspot detection and threshold calculation.

The nighttime fire detection algorithm for MODIS products (MOD14 and MYD14) begins with the pre-screening of pixels for clouds and water bodies (Fig. 3.4). Nighttime pixels are classified as cloudy if the condition, T_{12} (Brightness temperature at 12 µm) < 265 K, is satisfied. Water pixels are identified using 1- km resolution land sea mask contained in MODIS geolocation product. Next, the algorithm moves towards the elimination of obvious non-fire pixels and the identification of potential fire pixels. Pixels passing the tests, T_4 (Brightness temperature at 4 µm) > 305 K and $\Delta T > 10$ K ($\Delta T = T_4 - T_{11}$ (Brightness temperature at 11 µm)), are considered for further evaluation, whereas, the pixels failing these tests are immediately discarded. The algorithm then follows two logical paths for fire pixels identification.

The first path is the absolute threshold test, where a pixel is labelled as a fire pixel if $T_4 > 320$ K. The second path consists of a series of contextual tests. This path requires characterization of background pixels. Valid background pixels are searched in a window centered around the potential fire pixel and are defined as those not contaminated by cloud, are on-land and are not background fire pixels (having $T_4 > 310$ K and $\Delta T > 10$ K). The initial 3 × 3 window around the potential pixel can scale up to a 21 × 21 window to find required number of valid background pixels (should be at least 25% of pixels within the window and at least eight in number). Once sufficient number of valid background pixels are found, a series of statistical computations are done on them. μT_4 and δT_4 represent the mean and mean absolute deviation of T_4 for valid background pixels respectively, and, $\mu\Delta T$ and $\delta\Delta T$ represent the mean and mean absolute deviation of ΔT for valid background pixels respectively. Post the background characterization stage, three contextual tests are

done for relative fire detection (test 1: $\Delta T > \mu\Delta T + 3.5\ \delta\Delta T$, test 2: $\Delta T > \mu\Delta T + 6$ K and test 3: $T_4 > \mu T_4 + 3\ \delta T_4$). In the end, the potential pixel is identified definitively by the algorithm as a nighttime fire pixel, if the pixel passes either all three contextual tests or the absolute threshold test done earlier.

As mentioned earlier, the VAFP uses the equivalent of similar basic MODIS fire products algorithm described above for nocturnal fire detections (Csizar et. al 2014). While, VNF utilizes a SWIR band (VIIRS M10 band) as its primary detection band, nocturnal fire detections by VAFP and MODIS fire products (MOD14 and MYD14) are based on MWIR and LWIR bands. Since, the peak radiant emissions from gas flares are in SWIR, VNF is better suited to detect more gas flares. Another advantage that SWIR bands provide is that the background contribution to nighttime radiance in them is quite low compared to the detector noise that is recorded by them (Casadio and Arino 2008). The pixels containing hot sources stand out in these bands with their high radiance values and low contribution from background noise. Other than the choice of primary spectral band, another significant factor responsible for difference in hotspot detections is the treatment of clouds by these products. While MOD14, MYD14 and VAFP discard the pixels contaminated by clouds even partially, the VNF product doesn't discard the pixels with cloud cover. During examination of cloud mask, the developers of VNF product found that flares were consistently being misidentified as having cloud cover because of a spectral confusion and the pixels containing them were being marked as partially or completely cloudy (Elvidge et al. 2013). Therefore, a cloud-clearing algorithm was used in VNF to reset the cloud mask values for isolated cloud patches associated with M10 hot pixels

(potentially having flares in them). This enables an improved detection of flares by the VNF. VNF also uses a more stringent condition for removal of solar glint (solar zenith angle > 95º) compared to MODIS and VIIRS fire products (SZA ≥ 85º), which adds to reduction in error in nocturnal fire detection. Other known differences such as different spatial resolution of sensors and separate methods of potential pixel selection by their algorithm are also likely to contribute to hotspot detection differences amongst VNF, VAFP and MODIS fire products (Table 3.2).

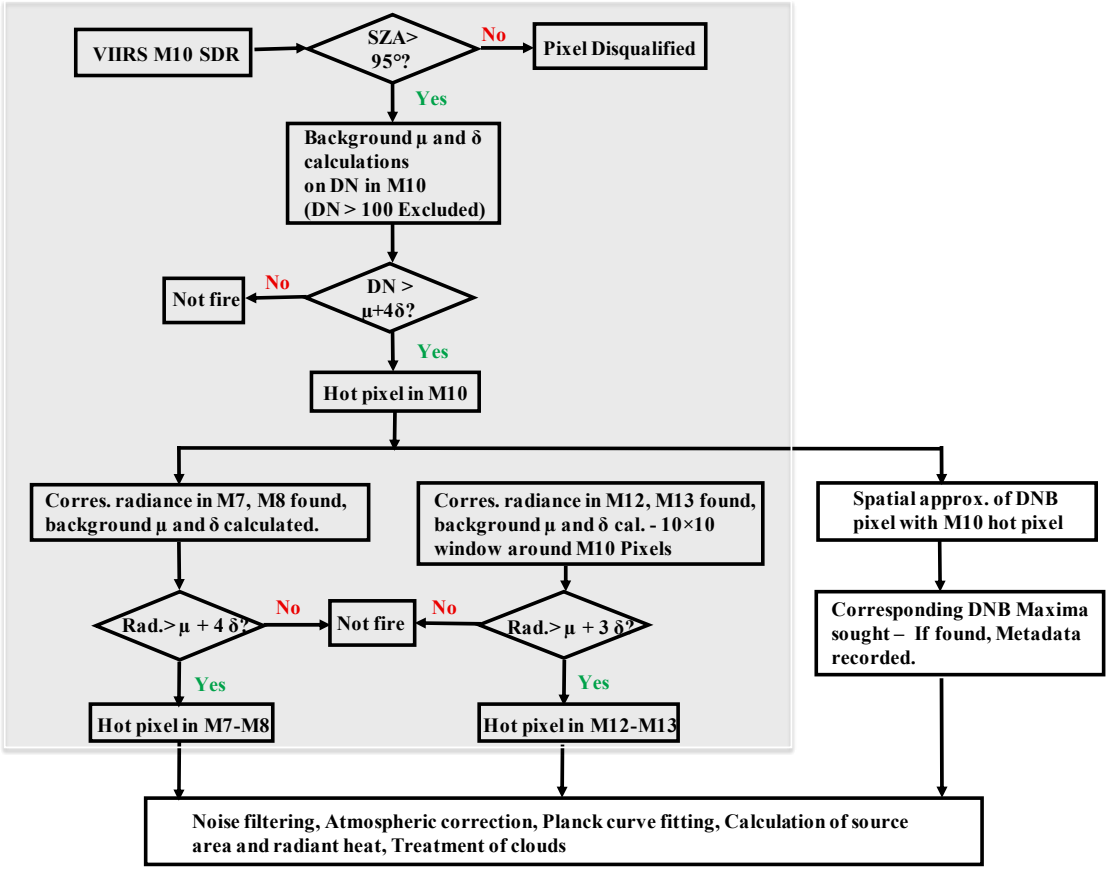

Figure 3.3 Flow chart of VNF Algorithm. Shaded part shows the part of algorithm used for replication in this study.

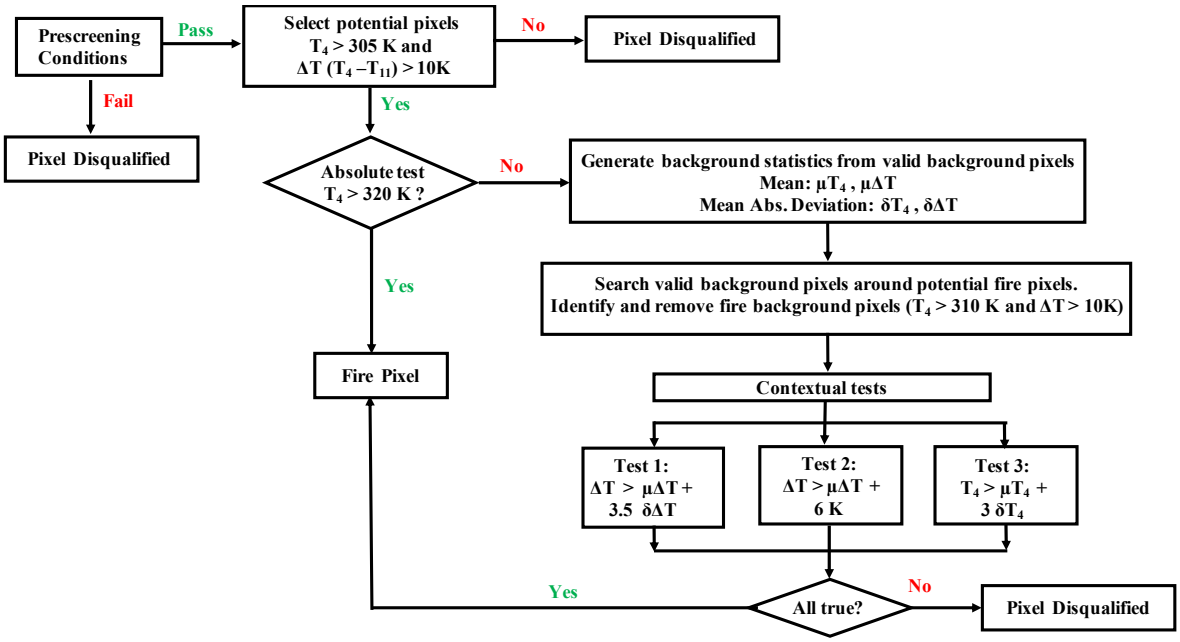

Figure 3.4 Flowchart of nighttime MODIS fire products algorithm.

Table 3.2 Differences in algorithms of tested fire products

	MOD14/MYD14	VAFP	VNF
Primary Detection Band	4µm , 11µm channels	4µm , 11µm channels	1.6µm channel
Treatment of Clouds	Cloudy Pixels Pre-screened	Cloudy Pixels Pre-screened	Completely or Partially Cloudy Pixel considered
Solar Contamination	Observations $\geq 85^0$ SZA	Observations $\geq 85^0$ SZA	Observations $> 95^0$ SZA
Auxiliary Info	Fire Radiative Power, Geolocation, Geometry	Geolocation, Geometry	Sub-pixel fire area , temperature and radiant heat, Geolocation, Geometry
Spatial Resolution	1 km at Nadir	750 m at Nadir	Variable
Aggregation	None	Sub-pixel aggregation across scan	N/A
Potential Pixel Selection	$T_4 > 305$ and $\Delta T > 10$	$T_4 > 305$ and $\Delta T > 10$	Radiance values above calculated threshold

3.2.3 The VNF-R product

The algorithm flow described in Section 3.2.2 (and shown in Fig. 3.1) was followed in an attempt to systematically replicate the VNF algorithm. The replicated product was named as VNF-R, where 'R' represents replica. A small sub-region of the study area showing hotspots persistently was chosen in Case Study I (Table 3.3) for replication and relevant VIIRS level-2 SDR data were collected for a random day. The VNF-R product was confined to threshold calculations and hotspot detections only. The VNF-R used level 2 SDR data from five VIIRS bands - M10, M7, M8, M12 and M13 to determine hotspots in these bands. These hotspots were then compared to the detections from VNF in respective bands. DNB wasn't used as it has a different pixel width than the M-bands and five bands were deemed sufficient from quality checks of the products. Maps were generated to demonstrate the similarities and differences in hotspot detections in each band by the two products within the test region. Section 4.2 discusses the results of replicating the VNF algorithm.

Table 3.3 Specifications of case studies.

Case Study	Date	Region	Purpose
I	05 May 2013	Latitude: 60.5° N - 60.8° N Longitude: 72.7° E – 73.0° E	Replication of VNF algorithm
II	04 July 2013	Latitude: 60° N - 61.5° N Longitude: 70.5° E - 72.0° E	Reconciliation between VAFP and VNF-R hotspots
III	02 August 2013	Latitude: 60.5° N - 61.5° N Longitude: 70.0° E – 71.0° E	Reconciliation between VAFP and VNF-R hotspots

3.3 Reconciliation between VAFP and VNF-R hotspots

Two case studies (Case Study II and Case Study III) were undertaken to compare and reconcile the hotspots detected by VAFP and VNF-R as a part of understanding of the hotspot detection differences between them (Table 3.3). These test days were chosen randomly from the set of days on which both VNF and VAFP detected fire activity (~20% of the total days studied) in the study region.

VNF-R was used instead of VNF as it gave more flexibility to work with dynamic thresholds in order to reconcile with the VAFP product detections. Additionally, some discrepancies in the VNF product were found while replicating it, so VNF-R was preferred over VNF for reconciliation cases. VAFP was chosen to compare to VNF-R as it had higher detections than MOD14 and MYD14 products for all months under study; hence, was deemed a better candidate for reconciliation cases. For reconciliation, threshold scaling analysis was done to see if the VNF-R detections in M10 band could be made to match with VAFP detections. The results of reconciliation case studies are discussed in Section 4.3.

3.4 Temperature and Fire Area Sensitivity Analysis

Since the detections by VAFP are mainly based on the 4 μm channel and the VNF is based on SWIR bands (principally M10 band centered on 1.6 μm), a simulation of radiance values in 4 μm and 1.6 μm channels was carried out for varying cases of temperatures and subpixel fire areas. The objective was to see how the top of the atmosphere (TOA) radiance seen by a sensor in these channels varies as the size of the fire contained in the pixel or the temperature of the fire changes. The TOA radiance, I, is represented as:

$$I = (1-A_f)\, I_b(\lambda,T_b) + (A_f)\, I_f(\lambda,T_f) \quad (3)$$

where A_f is the sub-pixel fire fraction, I_b is the spectral radiance ($W.sr^{-1}.m^{-2}.\mu m^{-1}$) contributed by the background pixels (computed by Planck function) and $I_f$represents the spectral radiance ($W.sr^{-1}.m^{-2}.\mu m^{-1}$) contributed by the flaming part of the pixel at the given wavelength. T_b and T_f represent surface kinetic temperatures of background and fire respectively (K). The background temperature was considered as 300 K uniformly for all simulations to represent average surface temperature during summer in West-Siberian, Russia (where the target region is located). Both the flaming part of the pixel and the background were considered as blackbodies (Giglio and Kendall 2001) and the atmospheric effects were neglected, so that computed radiances could represent TOA radiance values (Peterson et al. 2013). The subpixel fire fractions were varied from 0-100% and the temperatures were simulated for the range 1400-2000 K, to represent hot sources such as flares. Results of fire area and temperature sensitivity analysis are discussed in Section 4.4.

3.5 Evaluation of the VNF Product

As the VNF product proved to be more effective than other fire products in detecting gas flares by a considerable margin, the collected data (April - August 2013) were analyzed for further evaluation and validation of VNF. Ten known gas flaring locations were chosen within the test region boundaries and the efficacy of detection of these flares by VNF was studied. The detections where the distance between pixel center and the flare location exceeded 3 km were discarded and deemed as invalid. Many attributes such as fire area, fire temperature, viewing geometry, radiant heat, radiances in multiple bands, distance from actual flare location etc. associated with valid detections (distance < 3 km) were stored in a database for all 10 gas flaring sites for further evaluation. Histogram analysis of some important attributes such as view zenith angle (VZA), the angle between local zenith and the line of sight of satellite, was performed using the database to investigate if there was a viewing geometry preference associated with flare detections.

The mean subpixel fire areas reported by the VNF product for flares under study were also verified with Google Imagery. Triangular areas were drawn around the flare stacks over zoomed-in Google Imagery showing known flare locations and areas around the flares were calculated. It should be noted that the areas derived from Google Imagery are approximations of areas of the flares and are not representative of exact hot source areas as the size of flames emanating from flare stacks varies with factors like wind speed and fuel burned. Verification of areas could not be done for two locations of flares because of the limitation of the available zoomed-in Google Imagery there. In order to remove the bias from the outliers for mean area calculations from the VNF product, the interquartile range

($q_{0.25} - q_{0.75}$) of all recorded areas was used. The mean and the standard deviations were calculated using the data in this range only. Results associated with evaluation of the VNF product are discussed in Section 4.5.

4. Results

4.1 The gas flaring map and hotspot detection by multiple products

Preliminary tests demonstrated large differences between the detections done by the VNF product and MOD14, MYD14 & VAFP fire products over the study region (Fig. 2.1). A large number of these detections are presumably due to the gas flares prevalent in the test region. Following the procedure described in section 3.1 to demarcate gas flaring regions, a total of 99 cells (0.25° × 0.25° resolution) out of the 1600 cells within the test region were found to have satisfied the criteria of persistence and high temperature and thus were labelled as gas flaring regions. Fig. 4.1 and 4.2 show these demarcated gas flaring regions and depicts how detections from VNF, MOD14, MYD14 and VAFP products are aligned with them. Detections from VNF are shown separately in Fig. 4.1 due to the sheer ubiquity of them and because they form the basis of development of flaring map. A quantitative analysis of detections from all four products is tabulated in Table 4.1, displaying total number of detections within and outside the delineated gas flaring regions on a monthly basis. The number of nighttime hotspots detected by the VNF product is much higher than MODIS and VIIRS official fire products. VAFP (a distant follower of VNF in number of detections) exceeds MOD14 and MYD14 by almost a factor of five. In terms of alignment with the gas flaring areas, ~ 47% of nighttime detections from MOD14 are found to be within the gas flaring zones, whereas, ~ 67% and ~55% of nighttime detections by MYD14 and VAFP respectively are found in the gas flaring zones.

As described in Section 3.1, detection counts from the VNF product were divided into two categories based on associated brightness temperatures (T_B): (a) $T_B < 1600K$ and (b) $T_B \geq 1600K$; with category (b) representative of hotter sources such as gas flares. About 52% of the detections belonging to category (a) are found within the gas flaring zones and ~ 95% of the detections from category (b) are found within the flaring zones. Approximately 77% of the total number of valid detections by the VNF product over the entire study region belong to category (b) ($T_B \geq 1600$ K), which indicates the dominance of the flaring activity in the area.

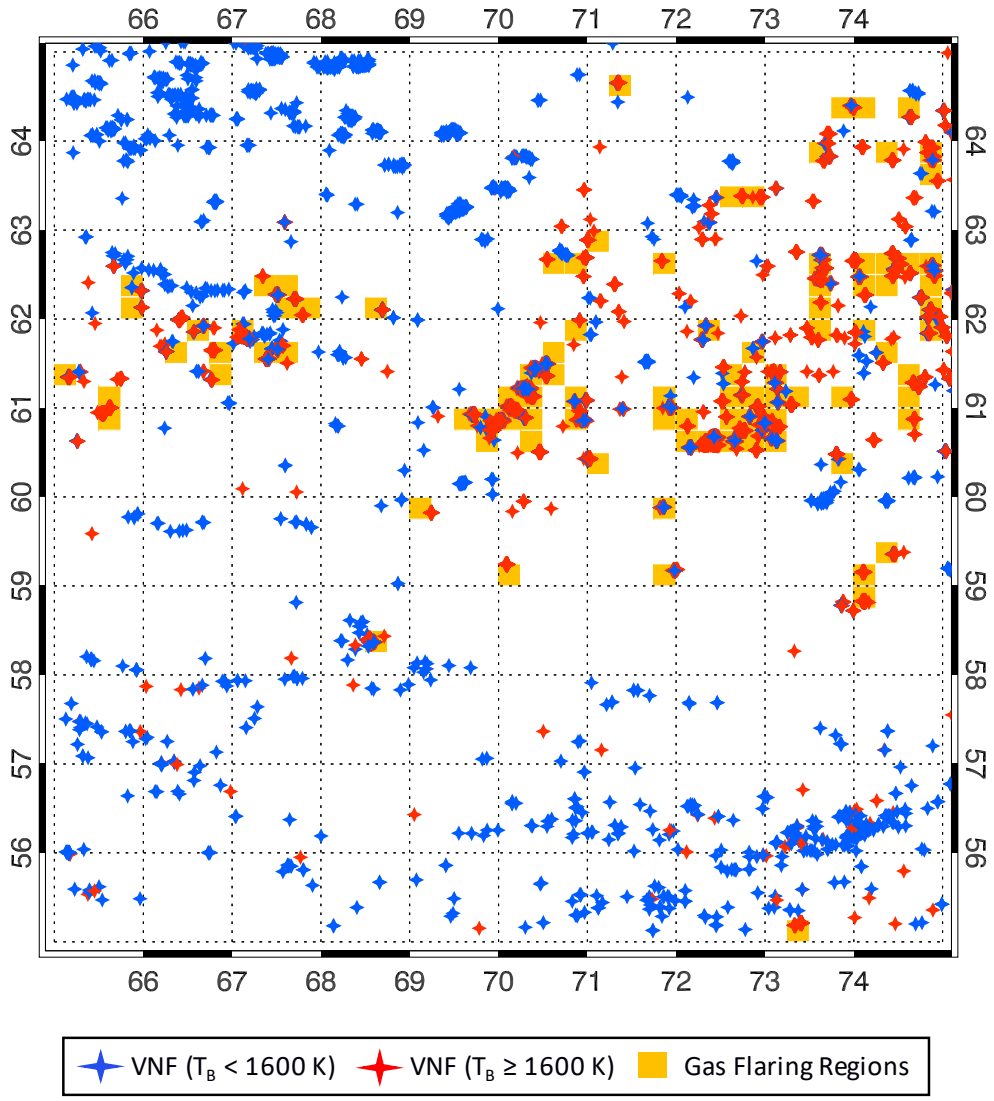

Figure 4.1 Nocturnal detections by VNF product over the gas flaring regions in the study area (April-August 2013).

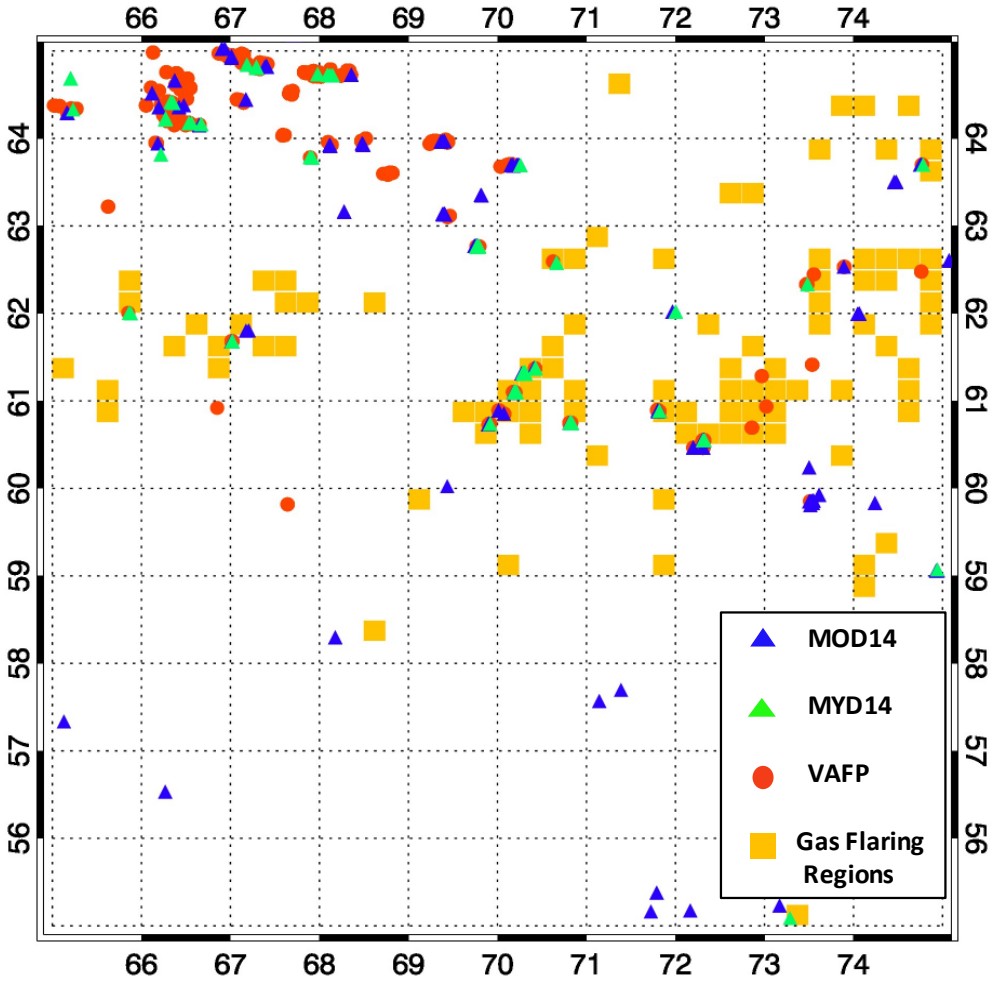

Figure 4.2 Nocturnal detections by MOD14, MYD14 and VAFP products over the gas flaring regions in the study area (April-August 2013)

Table 4.1 Multi-sensor fire detection during summer 2013 over the study area.

GFR* = Gas Flaring Regions shown in Fig. 4.1

Nighttime Fire Detections	MOD14 (MODIS Terra)			MYD14 (MODIS Aqua)			VAFP (VIIRS)			VNF T_B <1600K			VNF $T_B \geq$ 1600		
	Total	**In GFR**	**Out GFR**	**Total**	**In GFR**	**Out GFR**	**Total**	**In GFR**	**Out GFR**	**Total**	**In GFR**	**Out GFR**	**Total**	**In GFR**	**Out GFR**
April 2013	7	2	5	2	2	0	17	15	2	551	301	250	2603	2461	142
May 2013	11	7	4	1	1	0	45	45	0	339	161	178	1476	1400	76
June 2013	4	2	2	5	4	1	52	36	16	86	85	1	370	357	13
July 2013	56	23	33	49	26	23	314	137	177	983	569	414	3004	2897	107
Aug. 2013	59	30	29	27	23	4	138	81	57	1359	852	507	4952	4706	246

4.2 Replication of the VNF Algorithm

The test case for VNF replication (Case study I) shows that the VNF-R is able to detect the same number of total hotspots and at similar geolocations as detected by VNF in M10, M7, M8 and M13 bands for the test region on the test date. The detections; however, differ between the two in the M12 band where the VNF detects more hotspots than the VNF-R. Fig. 4.3 shows the detections done in the M10 band by both VNF and VNF-R. (The replication results for M7, M8, M12 and M13 bands are shown in Fig. 4.4 and Fig. 4.5).

Regardless of the similarities in hotspot detections between VNF and VNF-R in most M bands, the replication process brings forth some discrepancies in version 1.0 of the VNF product. As described in Section 3.2, to make hotspot detection more sensitive to different sample aggregation zones in VIIRS, three separate sets of thresholds are calculated for each aggregation zone in M10, M7 and M8 bands by the VNF algorithm. The case study; however, shows that the thresholds provided by the VNF product are inconsistent with the thresholds calculated by VNF-R as per the method described in Elvidge et al. (2013). For the M10 band, all ten detections from the VNF product are observed to have one threshold only, even though there is a change in the aggregation mode from 3:1 to 2:1 within the case study dataset. The VNF-R calculates two thresholds corresponding to the two aggregation modes and detects five hotspots each within pixels of both aggregation modes, satisfying their respective threshold criterion. The thresholds are expected to get higher as aggregation mode moves from 3:1 to 2:1 and then to 1:1 (Elvidge et al. 2013). Therefore, VNF product's constant threshold throughout the aggregation zones in M10 could lead to a serious miscalculation of surface hotspots. In the

M7 and M8 bands, although there are two thresholds provided by the VNF product corresponding to two aggregation modes in the case study dataset, the number of hotspots satisfying their respective threshold criterion differ between VNF and VNF-R for both the bands apart from slight difference in the calculated thresholds between the products. The discrepancies found in the M10, M7, and M8 bands for the test case are recorded in the Table 4.2. The M13 band shows a good fit between the two products with all hotspots detected at same geolocations and satisfying similar detection thresholds (as discussed in Section 3.2, the threshold calculations are different in M12, M13 bands than M7, M8 and M10 bands), whereas in M12 band, the VNF is found to overestimate the hotspots in M12 compared to VNF-R. M12 is the only band where the total number of hotspots and geolocations of hotspots differ between the VNF and VNF-R. The differences in M12 band detection could be stemming from additional processing steps that VNF algorithm does such as cloud correction and atmospheric filtering, but are not done in this study.

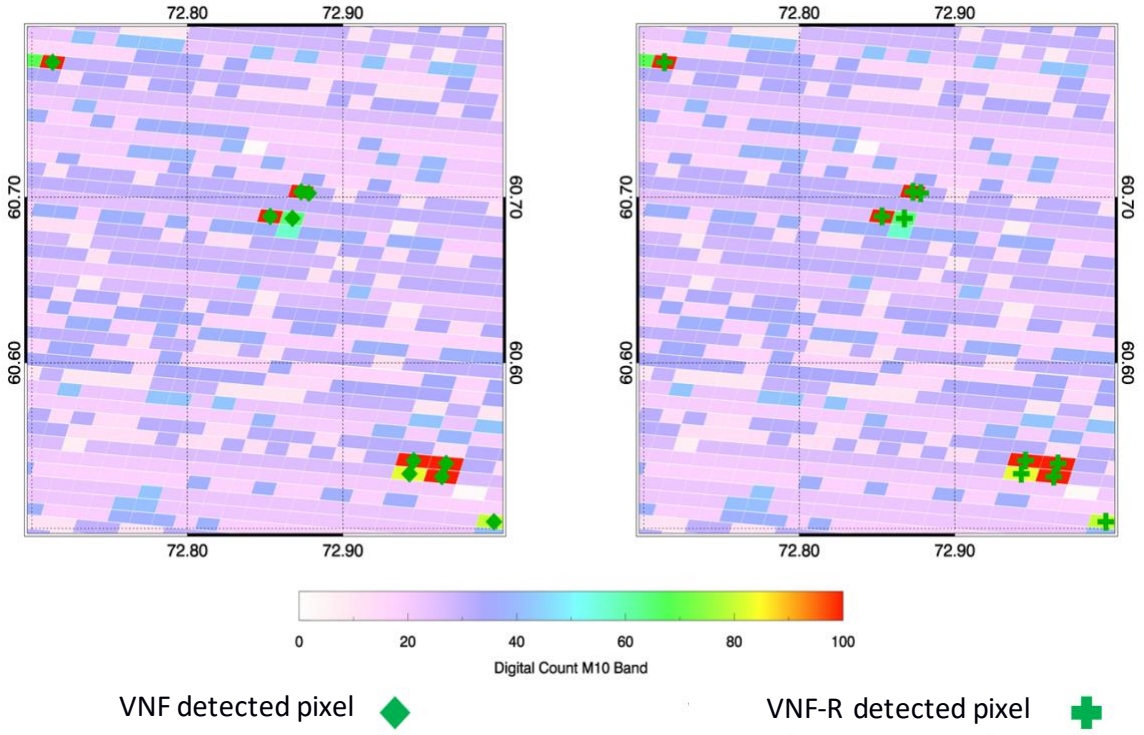

Figure 4.3 Case study I (5 May 2013): Replication of VNF product. VNF and VNF-R nighttime M10 detections.

a)

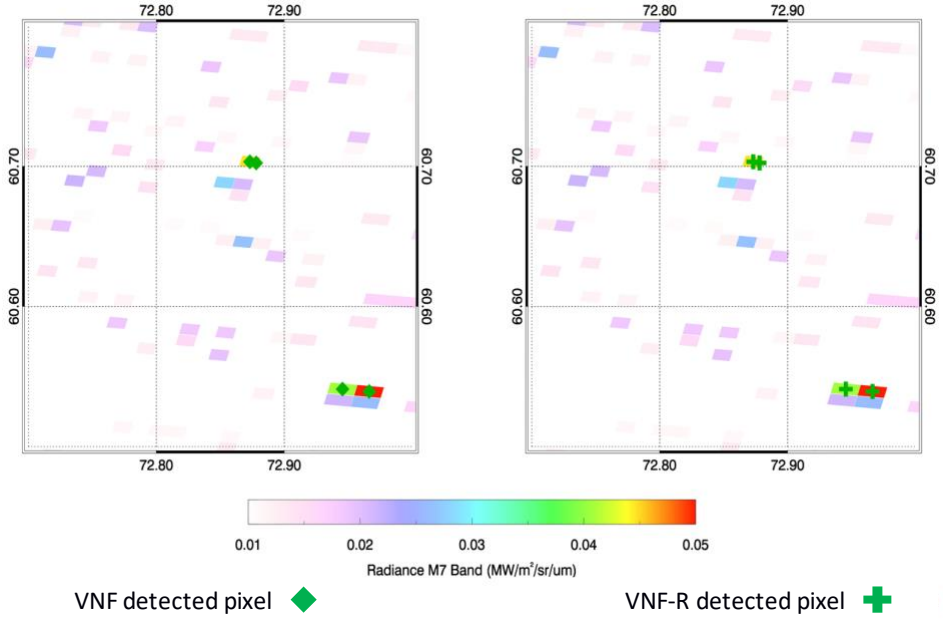

b)

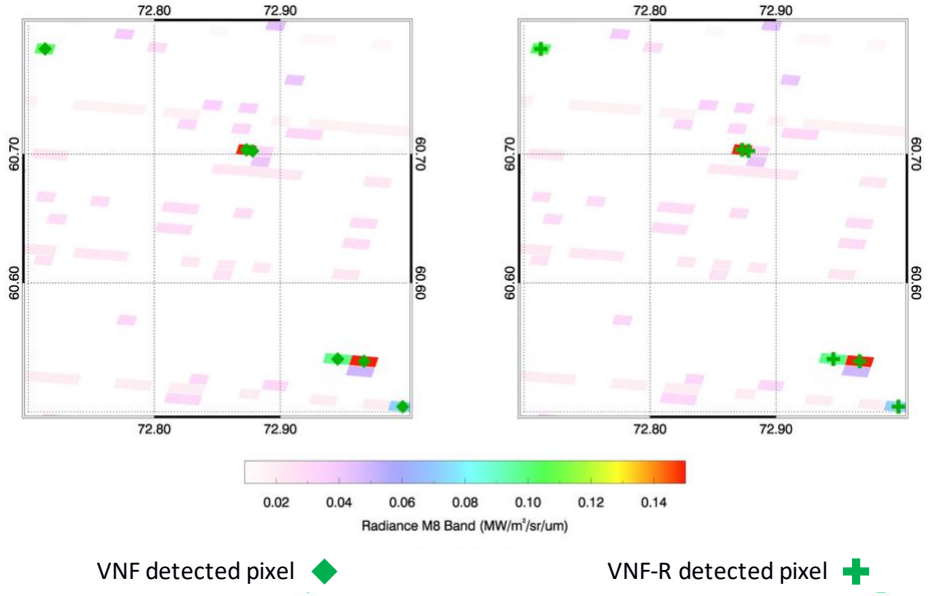

Figure 4.4 Case study I (5 May 2013): a) VNF and VNF-R nighttime M7 band detections. b) VNF and VNF-R nighttime M8 band detections.

a)

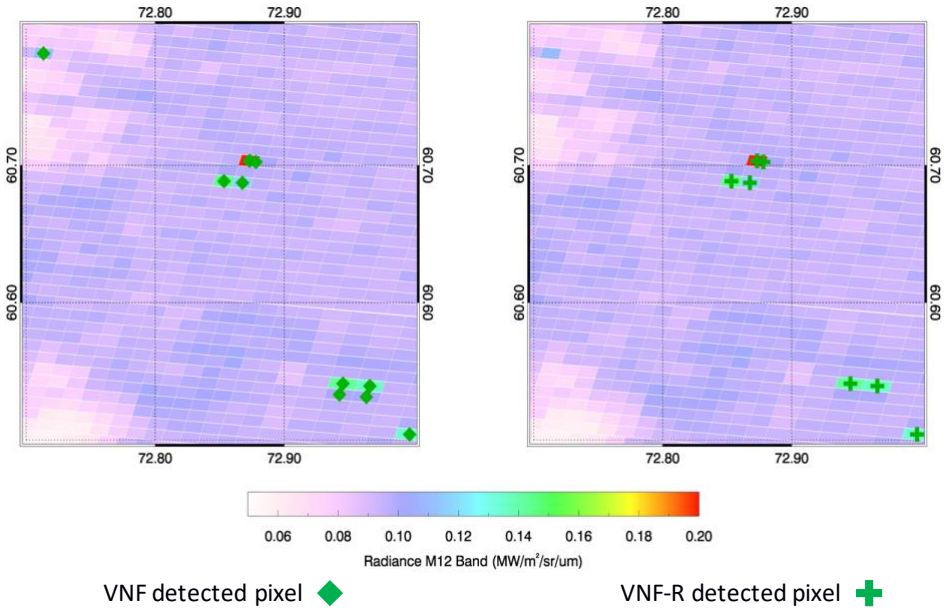

b)

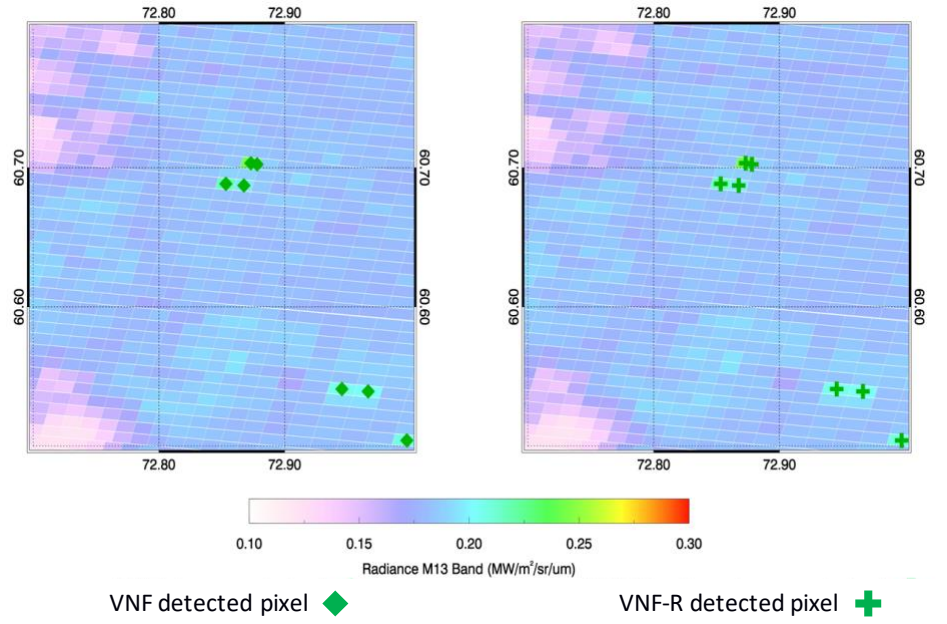

Figure 4.5 Case study I (5 May 2013): a) VNF and VNF-R nighttime M12 band detections. b) VNF and VNF-R nighttime M13 band detections.

Table 4.2 Case Study I: 05 May 2013. Differences between VNF algorithm and VNF-R using VIIRS level 2 data.

Differences between VNF and VNF-R	M10 (1.58 - 1.64 µm) Count	Threshold in DN	M07 (0.846 - 0.885 µm) Count	Threshold in Radiance ($MW/m^2/sr/\mu m$)	M08 (1.23 - 1.25 µm) Count	Threshold in Radiance ($MW/m^2/sr/\mu m$)
VNF (No Aggregation zone info. in VNF product)	10	57.80	1	0.030	2	0.060
	-	-	3	0.036	4	0.067
VNF-R (Aggregation zone 3:1)	5	56.03	2	0.034	3	0.060
(Aggregation zone 2:1)	5	59.58	2	0.037	3	0.071

4.3 Reconciliation between VAFP and VNF-R hotspots

For Case Study II, the VAFP detected two counts of nighttime fire within the test region, whereas the VNF-R detected 13 counts (Fig. 4.6a,c). VNF-R is used to study the detection differences with VAFP, as it enables scaling of dynamic thresholds (calculated from VIIRS level 2 SDR data as per the VNF algorithm). Fig. 4.6d shows detections from VNF-R in M10 band within the test region on the test date.

When the M10 threshold is augmented to five times, the original value, i.e., $5(\mu + 4\,\delta)$, out of a total of 13 detections earlier, only seven are able to withstand the new higher threshold (Fig. 4.6e). These 7 hotspots include the two hotspots that were detected by VAFP. When the M10 threshold is stepped up to 10 times the original value, VNF-R detections are reduced to four hotspots, still identifying the two hotspots seen by VAFP (Fig. 4.6f). As the threshold is increased to 30 times the original value in M10, the VNF-R detects only the exact two hotspots as VAFP did, indicating a convergence between the two products. One of the hotspots detected by VAFP and VNF-R shows what appears to be an industrial settlement when viewed with zoomed-in Google imagery (Fig. 4.6b) and there is a good probability of it being a flow station for gas flares. Additional zooming in did not allow the confirmation of a flow station. The other hotspot could not be verified as a flare because of the granularity of image in that location.

For Case Study III, four counts of fire were detected by the VAFP on the test date during nighttime within the test region, whereas VNF-R detected 30 hotspots on the same date within the test region (Fig. 4.7a,c). As in the previous case study, VNF-R is used to attempt reconciliation of hotspots between the VAFP and the VNF. Fig. 4.7d shows detections from VNF-R in M10 band within the test region on the test date.

When the M10 threshold is increased to 10 times the original value, only nine hotspots out of 30 detected earlier by VNF-R, satisfy the new higher threshold (Fig. 4.7e). These nine hotspots include the four hotspots that were detected by VAFP. When the M10 threshold is stepped up to 20 times the original value, VNF-R detections drop to six hotspots only, still containing the four hotspots seen by VAFP (Fig. 4.7f). A complete convergence between the two products doesn't occur using just the threshold scaling, as the six hotspots detected by VNF-R (Fig. 4.7f) keep persisting even when the original M10 threshold is stepped up higher than 20 times the original M10 value. At a significantly higher M10 threshold (70 times the original M10 value), the VNF-R hotspots recede to three in number, all of which are collocated with hotspots detected by the VAFP earlier. When observed through zoomed Google imagery, one of these three hotspots (picked up by VNF-R at all stepped up M10 thresholds and detected by VAFP) clearly shows a gas flare flow station within it (Fig. 4.7b).

The case studies indicate that even though VAFP is primarily designed for detecting bigger and cooler fires such as biomass burning, big gas flares could still be picked up by VAFP during the nighttime, and a corresponding local maxima in SWIR radiance values could assist in discriminating them from cooler fires. Additionally, Since the VNF-R was

able to match detections by VAFP by stepping up detection thresholds, it is probable (and worth probing) that lowering of VAFP's detection thresholds in known gas flaring regions could lead to more flare detections by VAFP and an appreciable match to VNF detections.

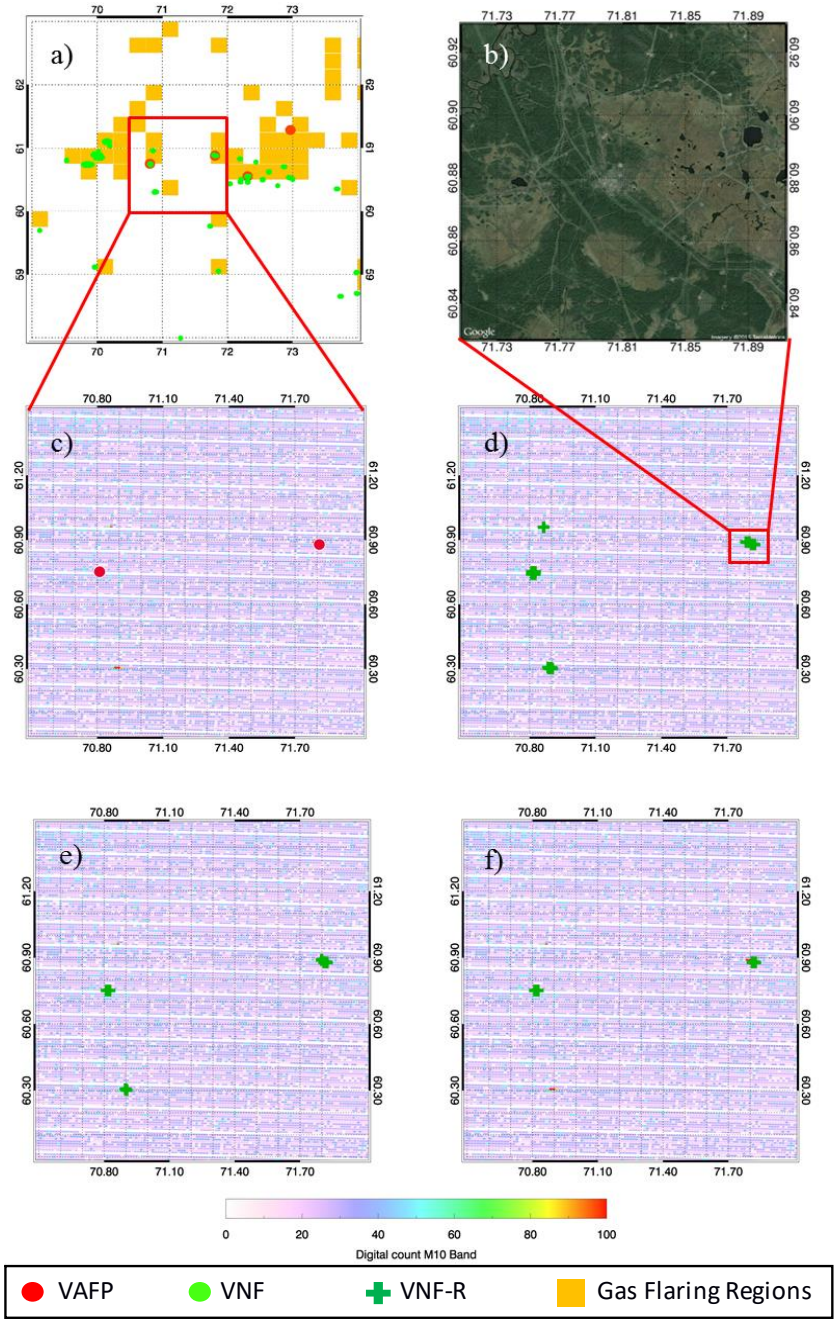

Figure 4.6 Case study II (4 July 2013): Reconciliation between VAFP and VNF-R. a) Demarcated gas flaring regions and detections by VAFP and VNF products on test date, red box highlights the test region. b) Satellite image of one of the hotspots within the test region showing presence of an industrial flare (Image courtesy: Google Maps). c) Detections by VAFP within the test region. d) Detections by VNF-R in M10 within the test region. e) Detections by VNF-R in M10 when threshold in (d) is stepped up by a factor of 5. f) Detections by VNF-R in M10 when threshold in (d) is stepped up by a factor of 10.

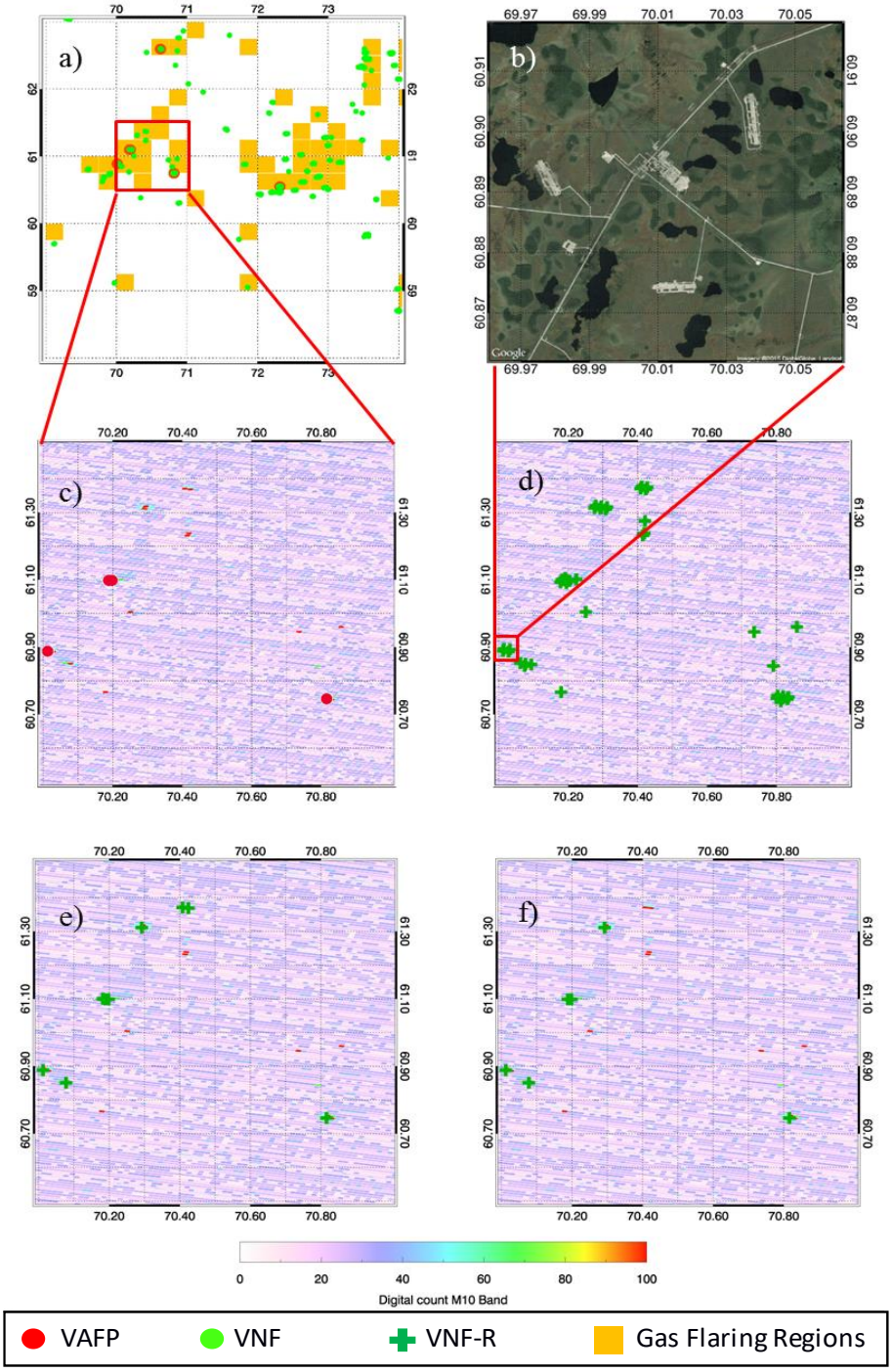

Figure 4.7 Case study III (2 August 2013): Reconciliation between VAFP and VNF-R. a) Demarcated gas flaring region and detections by VAFP and VNF products on test date, red box highlights the test region. b) Satellite image of one of the hotspots within the test region showing presence of industrial flare (Image courtesy: Google Maps). c) Detections by VAFP within the test region. d) Detections by VNF-R in M10 within the test region. e) Detections by VNF-R in M10 when threshold in (d) is stepped up by a factor of 10. f) Detections by VNF-R in M10 when threshold in (d) is stepped up by a factor of 20.

4.4 Temperature and Fire Area Sensitivity Analysis

As expected from applicable physics, the simulated 1.6 µm radiances increase in magnitude when both fire temperatures and subpixel fire area increase (Fig. 4.8a). 4 µm radiances also increase for high temperature fires with bigger areas (Fig. 4.8b), which explains the sensitivity seen in MWIR-based fire products towards bigger area gas flares (case studies demonstrated some large flares were also picked up by VAFP). However, as expected from Planck's law, the simulated 1.6 µm radiances are much higher in magnitude than the simulated 4 µm radiances for the same fire temperature and subpixel fire area increases.

Fig. 4.9 shows the difference of simulated 1.6 µm and 4 µm radiances against fire temperature and sub-pixel fire area changes. A clear cut-off point between the sensitivity of the two channels can be seen at fire temperatures nearing 1200 K. Beyond the cut-off point (towards higher temperatures), the difference between the 1.6 µm and 4 µm radiances is positive with the magnitude of difference increasing for hotter and bigger fires, whereas, below the cut-off point (towards lower temperatures), the simulated 4 µm radiances are higher than 1.6 µm counterparts. The higher sensitivity of 4 µm radiances below the cut-off point isn't surprising, as the peak radiation tends to shift to longer wavelengths ranges for sources with cooler temperatures.

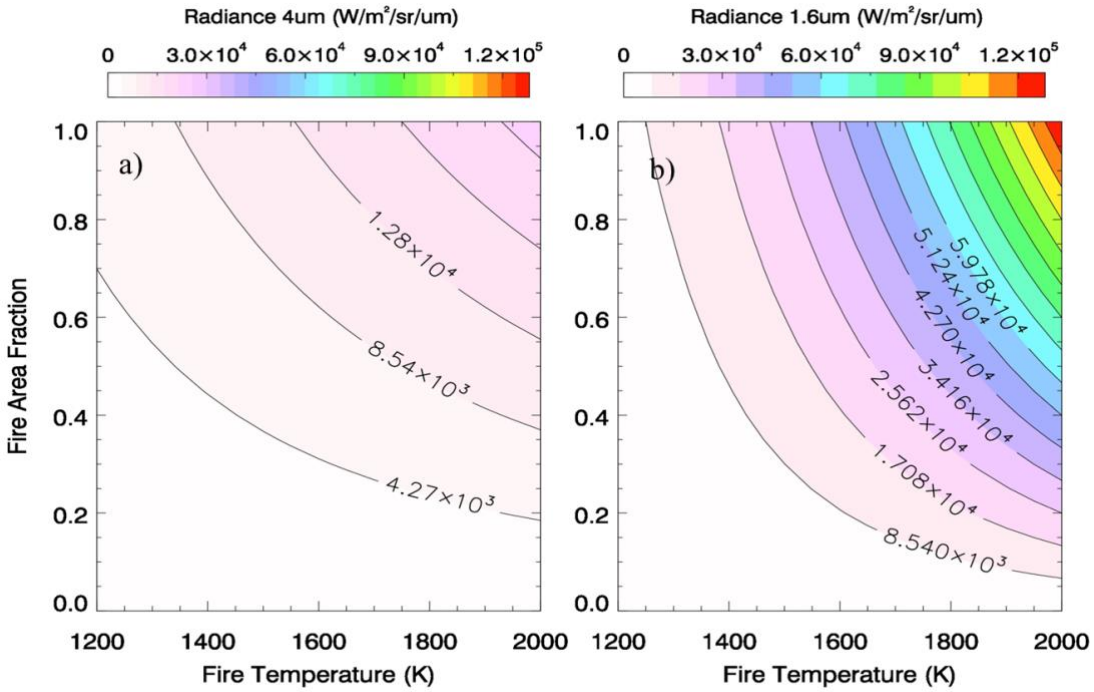

Figure 4.8 Simulation of a) 4 μm and b) 1.6 μm radiances for varying fire temperature and fire area fraction. The brightness temperature for background is considered uniformly at 300 K.

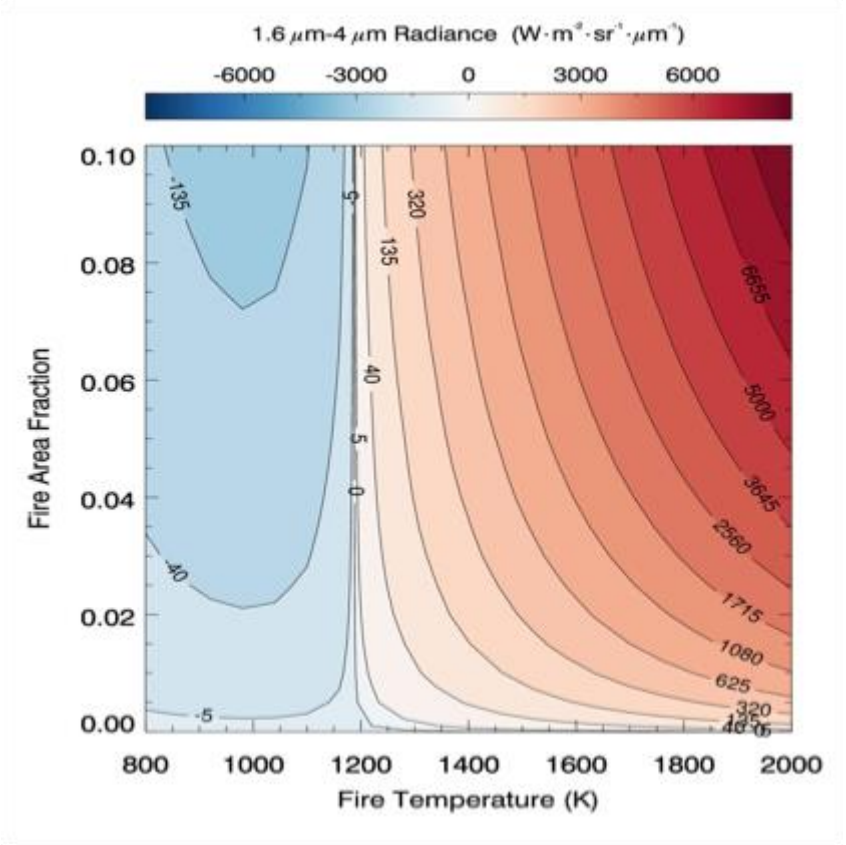

Figure 4.9 Simulation of difference between 1.6 µm and 4 µm radiances for varying fire temperature and fire area fraction.

4.5 Evaluation of the VNF product

The evaluation of the VNF product over ten test sites with known gas flares shows that the gas flares are detected with a reasonably high frequency by VNF at almost all test sites (eight of the flares were detected on 50 or more days of the total 153 days observed) (Table 4.3). The mean retrieved subpixel fire area for these sites vary from ~1 m^2 to ~25 m^2, demonstrating the efficacy of VNF in detecting gas flares of varying sizes. The flares were also detected by VNF sufficiently close to the actual flare sites (mean distance between detection by VNF and the actual site remained under 500 m for eight of the test sites). Fig. 4.10 shows these parameters detected by VNF between April - August 2013 over one of the ten tested flaring sites. The tested site was picked consistently by VNF (60 days out of total 153) and associated retrieved temperatures were representative of gas flares (mean detected temperature was 1894.10 K ± 223 K). Almost no detections were observed in the month of June, which could be due to heavy cloud cover and precipitation, since the region is known for abrupt changes in weather in summer and spring and receives higher rainfall in summer months. With the exception of one data point, the flare detection distance remained under 1km. The detected area by the VNF for the site showed some outliers and the uncertainties could be a further area of investigation regarding hot source detection of smaller flares.

Temperatures in the range of 1600-2000 K (typically associated with flares) were consistently observed with detections at each site studied. The histogram analysis of temperatures associated with valid detections shows a peak in the range of 1800-1900 K for most of the test sites (Fig. 4.11). The histogram analysis of VZA's shows that there is no preferred geometry for flare detections and flare detections are done at almost all VZA's

(except for very high angles > 70°), despite the small peak observed between observed 50°-60° for multiple flaring test sites (Fig. 4.12). The histogram points to the potential of VNF to detect flares across the range of viewing geometries.

The scatter-plot between mean area of test sites retrieved from VNF and areas of test sites estimated from Google imagery, shows a correlation of 0.91 (Fig. 4.13). The areas estimated by Google imagery are larger, in general, however is noteworthy that VNF tends to underestimate the areas of the flares and reports conservative estimates of hot source sizes based on Planck curve fitting.

Table 4.3 Using VNF for long term study of pre-determined flaring locations.

VIIRS VNF Test Sites	Geolocation (degrees)	# of Detections	Mean Fire Area (m^2)	Mean Retrieved Temperature (K)	Mean distance of detection (m)
Site 1:	Lat: 60.97 Lon: 73.85	45	4.59 ± 7.24	1773.71 ± 140.87	402.64 ± 327.47
Site 2:	Lat: 60.69 Lon: 72.86	62	5.37 ± 11.86	1789.61 ± 236.84	768.96 ± 697.08
Site 3:	Lat: 61.01 Lon:72.62	60	3.66 ± 2.09	1789.20 ± 109.47	420.56 ± 330.13
Site 4:	Lat: 61.64 Lon: 72.17	53	2.42 ± 2.18	1773.72 ± 226.36	370.54 ± 287.39
Site 5:	Lat: 61.28 Lon: 72.97	60	5.96 ± 6.32	1894.10 ± 223.00	333.06 ± 275.53
Site 6:	Lat: 60.78 Lon:72.70	53	3.23 ± 3.28	1710.96 ± 130.78	358.89 ± 226.84
Site 7:	Lat:62.45 Lon:73.55	56	11.04 ± 7.64	1728.12 ± 123.71	418.89 ± 476.16
Site 8:	Lat: 61.72 Lon:73.89	31	1.19 ± 0.78	1757.84 ± 154.92	505.73 ± 356.72
Site 9:	Lat: 62.49 Lon: 74.40	65	24.89 ± 16.49	1788.29 ± 90.11	344.19 ± 243.27
Site 10:	Lat: 60.74 Lon: 69.91	50	5.19 ± 4.04	1733.50 ± 131.16	480.738 ± 315.05

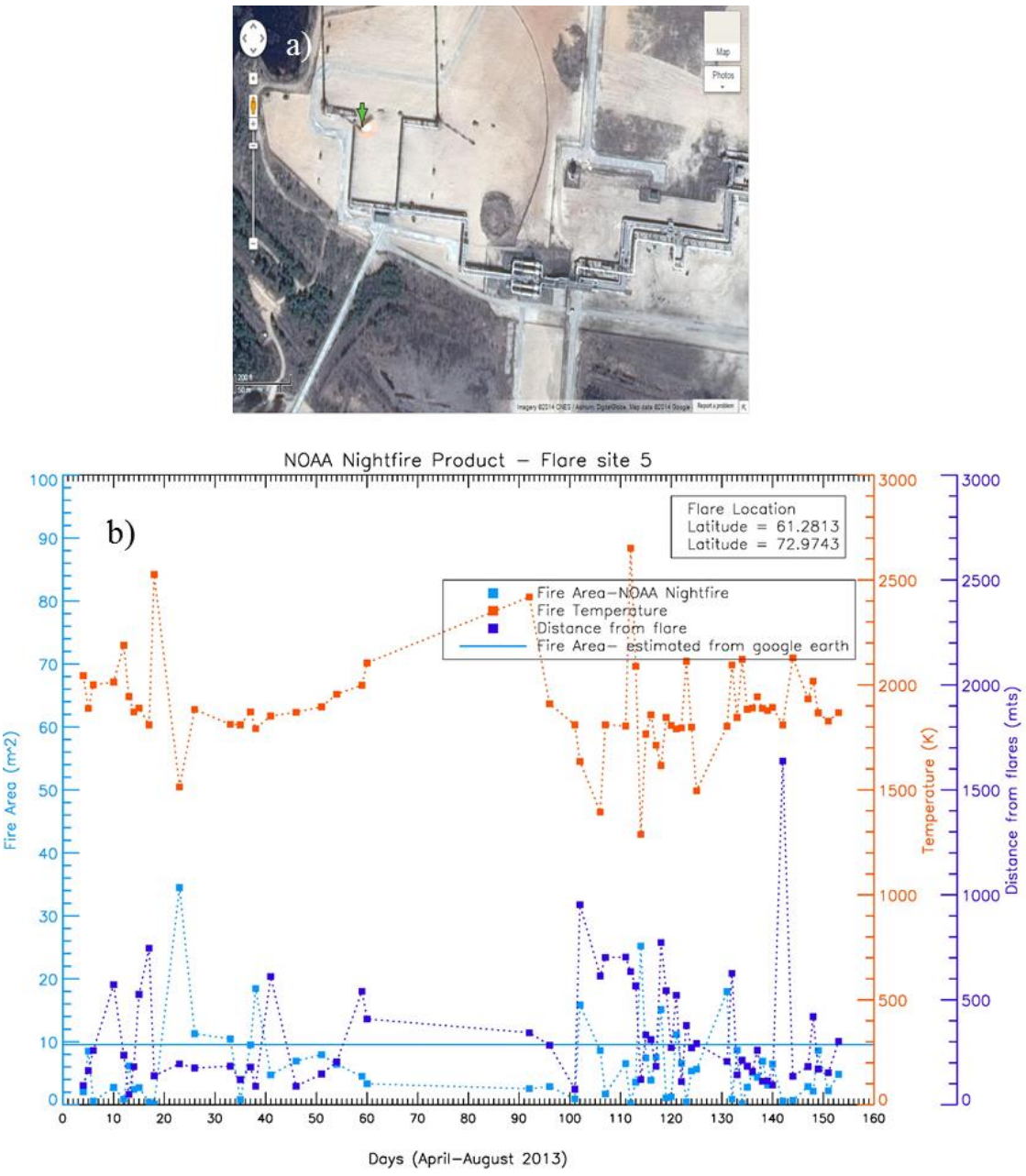

Figure 4.10 a) A test site in Khanty Mansiysk - Russia (Image courtesy: Google Maps). b) Fire area, temperature and distance of detected pixel from the flare location for this site over five months of 2013 retrieved from VNF (referred to as NOAA Nightfire in figure legend). The red lines represent the fire temperature reported by VNF for hotspots found in proximity to the flare, whereas the blue and navy blue lines represent the fire area and distance of flare from the centre of pixel detected, respectively.

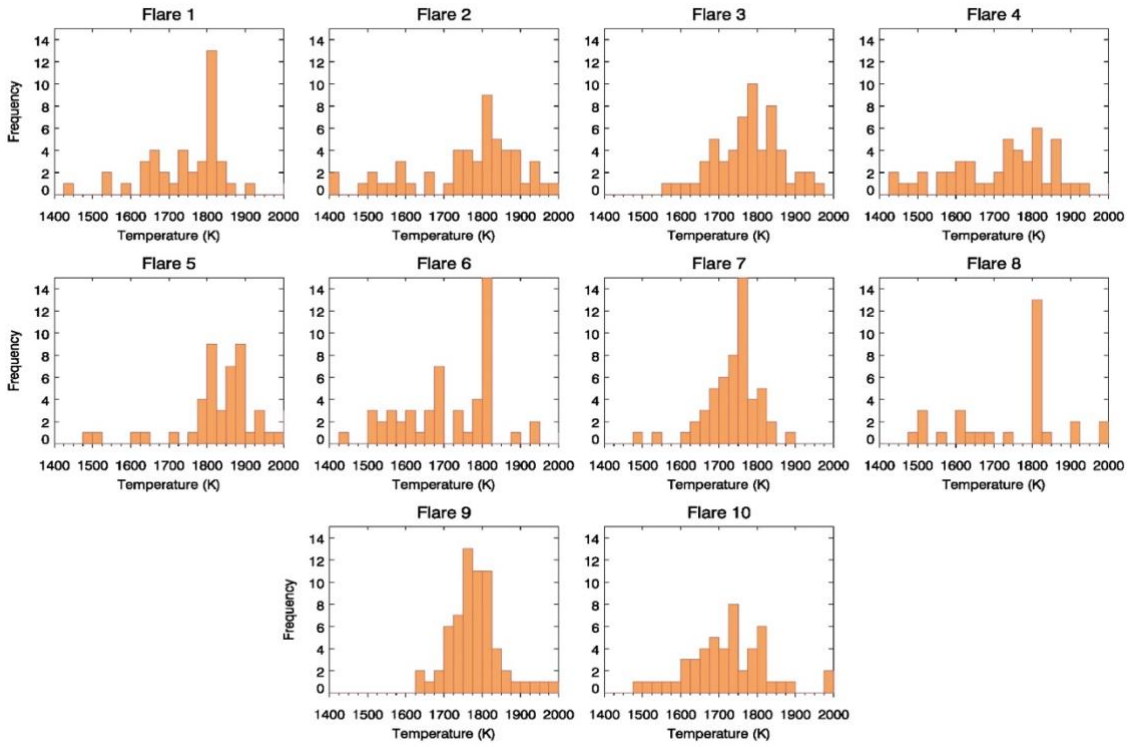

Figure 4.11 Histogram of fire temperatures reported by VNF for 10 test sites with flares over the five month period (Apr – Aug 2013).

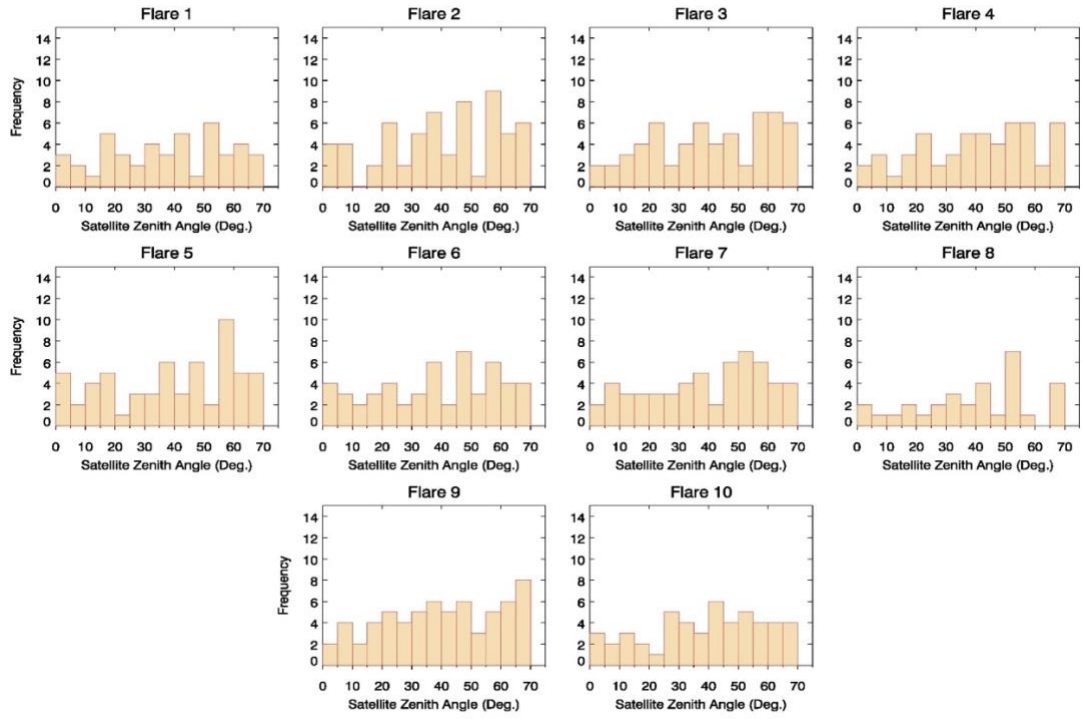

Figure 4.12 Histogram of view zenith angles reported by VNF for 10 test sites with flares over the five month period (Apr - Aug) 2013.

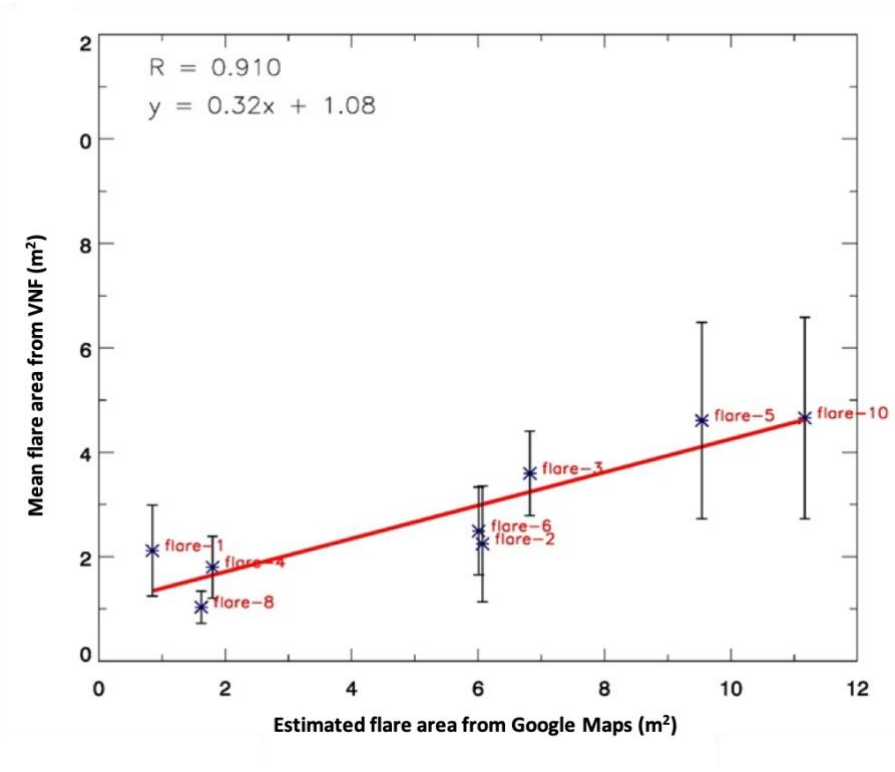

Figure 4.13 Scatterplot of fire areas reported by VNF for different flare sites vs the area estimated using google imagery for the respective sites.

5. Summary & Conclusions

Satellite-based fire detection products were tested for their hotspot detection capability over a large gas flaring region in Russia for the time period of April-August 2013. The analyses showed that the VNF product detected the greatest amount of nighttime gas flaring activity in the study region. A broad gas flaring map was developed using VNF data that highlights the cells in the study region with persistent flaring activity. The fire counts observed by the VNF product were much higher than the other products tested (MOD14, MYD14, VAFP) both within and outside the demarcated gas flaring zones. The strikingly large differences in hotspot detection between VNF and other products could be attributed to the choice of the primary detection band, among other factors, which are highlighted in Table 3.2.

The VNF algorithm was replicated using multispectral VIIRS level-2 SDR data in an attempt to better understand its function. A case study involving systematic replication of the VNF algorithm revealed discrepancies between the thresholds calculated for different bands by the VNF product (version 1.0) and by the replicated product VNF-R (which is based on theoretical methods described by the developers). Most notably in the M10 band, all the detections from the VNF product were observed to have one threshold, even though the sample aggregation mode changed from 3:1 to 2:1 within the case study dataset, which meant that a distinct higher threshold was expected for the pixels of 2:1 sample aggregation. These discrepancies in threshold calculations by the VNF product should be investigated for corrections, as they could lead to a serious miscalculation of surface hotspots.

Case studies seeking to reconcile the hotspot detection differences between the VNF-R and VAFP products show that upon increasing the hot spot detection thresholds (M10 based) manifold, the VNF-R was able to match the detections from VAFP. The factor by which thresholds for VNF-R needed to be multiplied to match with VAFP was found to be variable between the two case studies. However, as the VNF-R was able to match the detections by VAFP by stepping up detection thresholds, it is possible that lowering of VAFP's detection thresholds in known gas flaring regions could lead to more flare detections by VAFP and an appreciable match to VNF detections could be achieved. The case studies also demonstrated that despite being primarily designed for detecting bigger and cooler fires such as biomass burning, large gas flares could still be picked up by VAFP during the nighttime, and a corresponding local maxima in SWIR radiance values could aid in discriminating them from cooler fires.

In order to evaluate the performance of the VNF product to detect flares over a longer period of time, the product was tested on known flaring locations for a period of 5 months (April-August 2013). A database was created using data associated with flare detections by the product for the test sites. The database included information such as viewing geometries, brightness temperatures, fire areas and multispectral radiances. An analysis of the database revealed some of the characteristic features of the flares, e.g., the temperatures associated with detected flares were consistently observed to be greater than 1600 K. There seemed to be no view zenith angle preference for the detections of flares as the flare hotspots were reported for a wide entire range of VZAs. The mean areas of detected flares reported by VNF were compared to areas estimated with Google Imagery

and it was observed that VNF generally underestimates the area of the flares. Overall, the product did sufficiently well in detecting all the test flares with frequency of detection of flares varying between 20% to 42% of the days tested. Expectedly, the lowest and highest frequency of detection were for the smallest and largest area flare tested respectively. The high frequency of detection of pre-determined flaring sites corroborates VNF's proficiency in hotspot detection in gas flaring regions.

Taking into account VNF's ability to detect gas flares efficiently, long-term data from VNF could be obtained in the future to form a database that could potentially be used for developing an objective gas flare mapping algorithm by employing unsupervised clustering techniques. The long-term observation of multispectral radiances associated with flares could be used to determine the minimum thresholds to prescreen pixels in SWIR bands and for establishing characteristic radiances of flares in SWIR bands for similarity assessment and labelling in post clustering stages. The minimum threshold for the potential pixel selection could be computed by assessing SWIR radiances from all observed flare sites in the database. Such prescreening of potential pixels could make the ensuing clustering algorithm much less computationally intensive. The clustering (grouping of pixels) operation could then be performed individually in each band and subsequently the clusters having similar spectral features (radiance values) as reported from database could be identified in each band. The iterative optimization or migrating means clustering algorithm could be used for this purpose. The advantage of using an unsupervised algorithm is that no foreknowledge of classes is required and thus it saves considerable time used in manual identification of spectral features. After the clustering process is complete, spectral means of all clusters from each band could be compared to the

characteristic radiance value stored in the database of the respective bands for similarity assessment. The pixels belonging to the cluster displaying maximum similarity to the database counterparts could then be labelled as hot pixels in their respective SWIR band. Pixels labelled hot in multiple bands could then be identified as gas flaring regions. The development of such an objective gas flaring algorithm would significantly help in reducing uncertainties in highly important domains such as gas flare emissions inventories, contribution of flare emissions to global carbon budget, global energy usage, policy assessment and formulation of regulations in gas flaring regions.

6. Updates

The research for this study was completed in July 2015. This chapter presents some important updates related to this work that have occurred between the period of completion of research work and publication of this thesis. The research work related to this thesis was published in 2017 (Sharma et al. 2017). The histogram of view zenith angles for test flares detected by VNF (Figure 10 in Sharma et al. (2017) was found to be erroneous due to an anomalous calculation and a corrected version is included in the thesis (Fig. 4.11). Some minor aberrations related to hot spot numbers in figures related to case study for reconciliation between VNF-R and VAFP are also corrected in the thesis (Section 4.1 and Figure 6 in Sharma et al. (2017) vs. Section 4.3 and Fig. 4.6 in the thesis).

The datasets used in the study have been upgraded to newer versions. MOD14/MYD14 were upgraded with the availability of MODIS collection 6 active products (Giglio et al. 2016). MODIS collection 6 products have been available since September 2015 and now offer coverage from November 2000 (for Terra) and from July 2002 (for Aqua) to the present. Archiving of VAFP was discontinued at NOAA CLASS after 28 June 2017 and a higher quality replacement product, JPSS active fire, based on MODIS Collection 6 algorithm is available from the National Center for Environmental Information (NCEI 2019) from 15 March 2016 to the present. VNF's new version, V3.0, is archived at NGDC and is available from December 2017 to the present. Another version of VNF, 2.1, is also available from NGDC (NGDC 2019), covering the time period of March 2012 to December 2017.

Some recent notable advances related to gas flaring characterization from space and using VNF for various purposes are summarized below.

Caseiro et al. (2018) adapted a VNF algorithm for the characterization of persistent hotspots using observations from the Sea and Land Surface Temperature Radiometer (SLSTR) on-board the Copernicus Sentinel-3 satellite. The main differences between the newly adapted algorithm and the original VNF algorithm are the use of a non-statistical contextual methodology for hotspot detection that is independent of the number of hot sources present and their intensity, analysis of integrated radiances from clusters of hotspots rather than from individual pixels, and the correction of co-registration errors between hot source clusters in different spectral bands. Clustering was done to address interference of signal from a single hot pixel to adjacent pixels and was considered a more realistic way representing gas flaring facilities with large arrays of gas flares. The algorithm used two SWIR channels from SLSTR, S5 and S6 (centered at 1.61 μm and 2.25 μm respectively). Hotspot detections below the detection limits of M10 in Elvidge et al. (2013) were found in both SLSTR SWIR channels which indicated a capability for detecting smaller flares than detected by the original VNF product. The authors also suggested the ability for a better characterization of smaller gas flares through using Planck curve fitting, on account of presence of an extra SWIR channel compared to VNF methodology.

On comparing VNF detections with SLSTR detections over several test regions (North Sea, Caspian Sea, Persian Gulf and West Africa) for a variable duration in the latter half of 2016, VNF product was found to detect more hotspots. The result was attributed to a larger swath width (3040 km for VIIRS vs 1420 km for SLSTR), shorter revisit time and the detection of single pixels by VNF against the detection of contiguous clusters by this

work. The SLSTR computed temperatures were found to be slightly lower and the source areas were found to be slightly larger compared to VNF product. The difference in algorithms (analyzing clusters instead of single hot pixel) was considered the reason for this result. Persistent flaring locations detected by both products were found to be highly similar for all four tested areas. A single site study was also done for a flaring site in Yamal Peninsula in Siberia between December 2016 and January 2017. VNF product was found to detect more hotspots and computed slightly higher temperatures than SLSTR, although the computed hot source areas were similar for both products for the single site case.

Faruolo et al. (2018) used a framework of MODIS based method for the detection of hotspots and the computation of gas flare volume called RST-FLARE. RST-FLARE is a specific configuration of Robust Satellite Techniques (RST) used for monitoring major environmental and industrial hazards (Tramutoli 2007; Faruolo et al. 2014). The three key steps of RST-FLARE include: detection of flare sites, computation of source emissive power, and gas flare volume estimation. The algorithm was tested for the Niger Delta region, well-known for significant gas flaring, for the period of 2000-2016. When RST-FLARE detections were compared to detections from VNF (data obtained for 2012-2016), 95% of flaring sites were detected by both products regardless of differences in temporal aggregation (17 years of data aggregated on an annual scale by RST-FLARE vs five years of VNF data aggregated on monthly scale). Despite being MWIR based, the success in detection of gas flares was attributed to a differential, self-adaptive algorithm that used locally derived thresholds in spatio-temporal domains rather than fixed thresholds. It was suggested that the unmatched detections between the two products could be helpful in figuring out false positives in flare detections in future.

Franklin et al. (2019) used VNF to characterize flaring in the Eagle Ford Shale region of South Texas, from April 2012 to December 2016. The authors used the VNF product V2.1 to apply a spatiotemporal hierarchical clustering technique to determine gas flaring locations and filter isolated observations. Clustered VNF flares were then associated with flared gas volumes reported by Railroad Commission of Texas (TXRRC) at the county level. Subsequently, estimates of flared gas volumes at each flaring site were made using a regression model that linked VNF reported parameters (fire temperature, source area, radiant heat) to TXRRC reported flare volumes. The results show that VNF data can be exploited in future at a local scale for important applications in air quality monitoring, inventory emission estimation and regulatory analyses.

More recently Elvidge et al. (2019), the developers of the original VNF algorithm, examined detection limits of combustion sources of nighttime VIIRS bands in Near-IR (M7, M8), SWIR (M10, M11), MWIR (M12, M13) and DNB. A global analysis of VNF data for January 2018 (first month where S-NPP VIIRS collected data in M11 spectral band at night) revealed that inclusion of NIR and SWIR channels resulted in two-fold increase of VNF detections with temperature fits compared to detections involving MWIR. The detection capability for hot sources with small areas was found to be enhanced across a wide range of temperatures due to the addition of SWIR bands. The DNB detection limits for hot sources were found to be even lower, enabling it to detect much smaller combustion sources for temperatures mimicking gas flares. A test case study for India in 2015 showed that detections in DNB were 15 times more than detections by VNF. It is suggested that low detection limits from DNB could be useful in detecting hot sources that are not detected by VNF.

Some crucial updates on the VNF algorithm are also mentioned in Elvidge et al. (2019). An important development is the inclusion of another SWIR band, M11, centered at 2.2 μm, in the VNF algorithm. For processing in VNF records, the detections are required to be found in SWIR and MWIR bands i.e., detections in M7, M8 not seen in MWIR or SWIR are discarded. Detections in M12 and M13 are now done using scattergram images of M12, M13. IR sources in these bands are identified as outliers outside of the dense diagonal cloud of pixels which corresponds to temperature variations of background in the scattergram.

Identification of error sources in VNF and means of correction are also presented in this work. Bow-tie effect (ground footprint overlap in adjacent lines, especially pronounced in 1:1 aggregation zone of swath) in VNF is filtered by requiring detections in adjacent scans to be at least half a pixel apart. Subpixel saturation, primarily found in the M12 band and somewhat in M11 band, is addressed by identification of saturated pixels by the updated algorithm pointing out the irregularities in radiances and their removal from Planck curve fitting. Almost all bands in VNF are subject to errors introduced due to high energy particle detections (HEPD), particularly in the South Atlantic Anomaly (SAA) region. HEPD related errors are handled by requiring VNF detection in multiple spectral bands, as it is unlikely that pixels have simultaneous HEPD in multiple spectral bands. The authors found that the exclusion of isolated M11-only detections largely removed HEPD related errors, a similar filtering algorithm is suggested, though not yet implemented, for the M12, M13 bands which are indicated to be responsible for most HEPD related errors in VNF along with M11.

Recent developments highlighted above substantiate the continuing and important role of VNF in global gas flare monitoring with unprecedented accuracy and assessment of related emissions. In addition, the use of multispectral data from other satellite sensors to adapt and implement VNF algorithms, the strong agreement by recent works on persistent flaring locations detected by VNF, the exploitation of VNF data for estimation of gas flares volumes at regional and local scale, and finally, the refinement in VNF algorithms and their findings extend the capabilities in hot source detection and characterization using unexploited VIIRS spectral channels such as DNB and M11. emissions.

REFERENCES

ADMHMAO, 2019: Geographical location: Khanty-Mansiysk Autonomous Okrug-Ugra. Official Site of Public Authorities, Accessed August 7 2019, https://admhmao.ru/en/about/general/geo/

Ahmad, S., V. Salomonson, W. Barnes, X. Xiong, G. Leptoukh, and G. Serafino, 2002: MODIS radiances and reflectances for earth system science studies and environmental applications. American Meteorological Society, 192 pp.

Anejionu, O. C. D., G. A. Blackburn, and J. D. Whyatt, 2015: Detecting gas flares and estimating flaring volumes at individual flow stations using MODIS data. *Remote Sens.Environ.*, **158**, 81-94, doi:10.1016/j.rse.2014.11.018.

Anejionu, O. C. D., G. A. Blackburn, and J. D. Whyatt, 2014: Satellite survey of gas flares: development and application of a Landsat-based technique in the Niger Delta. *Int.J.Remote Sens.*, **35**, 1900-1925, doi:10.1080/01431161.2013.879351.

Cao, C., F. J. De Luccia, X. Xiong, R. Wolfe, and F. Weng, 2014: Early On-Orbit Performance of the visible infrared imaging radiometer suite onboard the Suomi National Polar-Orbiting Partnership (S-NPP) satellite. *IEEE Trans.Geosci.Remote Sens.*, **52**, 1142-1156, doi:10.1109/TGRS.2013.2247768.

Casadio, S., O. Arino, and A. Minchella, 2012a: Use of ATSR and SAR measurements for the monitoring and characterisation of night-time gas flaring from off-shore platforms: The North Sea test case. *Remote Sens.Environ.*, **123**, 175-186, doi:10.1016/j.rse.2012.03.021.

Casadio, S., O. Arino, and D. Serpe, 2012b: Gas flaring monitoring from space using the ATSR instrument series. *Remote Sens.Environ.,* **116**, 239-249, doi:10.1016/j.rse.2010.11.022.

Casadio, S., O. Arino, 2008: ATSR-WFA new algorithms for hot spot detection Proceedings of 2nd MERIS-AATSR workshop, September 22–26, ESRIN, ESA Publication (2008)

Caseiro, A., G. Ruecker, J. Tiemann, D. Leimbach, E. Lorenz, O. Frauenberger, and J. W. Kaiser, 2018: Persistent hot spot detection and characterisation using SLSTR. *Remote Sens.,* **10**, 1118, doi:10.3390/rs10071118.

CLASS, 2014: VIIRS Active Fire EDR (AVAFO), distributed by NOAA's Comprehensive Large Array-data Stewardship System, Accessed 7 August 2019, https://www.bou.class.noaa.gov/saa/products/catSearch.

Croft, T., 1978: Nighttime images of earth from space. *Sci.Am.,* **239**, 86-&.

Croft, T., 1973: Burning waste gas in oil fields. *Nature,* **245**, 375-376, doi:10.1038/245375a0.

Csiszar, I., W. Schroeder, L. Giglio, E. Ellicott, K. P. Vadrevu, C. O. Justice, and B. Wind, 2014: Active fires from the Suomi NPP visible infrared imaging radiometer suite: Product status and first evaluation results. *Journal of Geophysical Research-Atmospheres,* **119**, 803-816, doi:10.1002/2013JD020453.

Elvidge, C. D., M. Zhizhin, K. Baugh, F. C. Hsu, and T. Ghosh, 2019: Extending nighttime combustion source detection limits with short wavelength VIIRS data. *Remote Sens.,* **11**, 395, doi:10.3390/rs11040395.

Elvidge, C. D., M. Zhizhin, F. Hsu, and K. E. Baugh, 2013: VIIRS Nightfire: Satellite pyrometry at night. *Remote Sensing,* **5**, 4423-4449, doi:10.3390/rs5094423.

Elvidge, C. D., D. Ziskin, K. E. Baugh, B. T. Tuttle, T. Ghosh, D. W. Pack, E. H. Erwin, and M. Zhizhin, 2009: A fifteen year record of global natural gas flaring derived from satellite data. *Energies,* **2**, 595-622, doi:10.3390/en20300595.

Elvidge, C. D., E. H. Erwin, K. E. Baugh, B. T. Tuttle, A. T. Howard, D. W. Pack, and C. Milesi, 2007: Satellite data estimate worldwide flared gas volumes. *Oil & Gas Journal,* **105**, 50-+.

Elvidge, C., M. Imhoff, K. Baugh, V. Hobson, I. Nelson, J. Safran, J. Dietz, and B. Tuttle, 2001: Night-time lights of the world: 1994-1995. *Isprs Journal of Photogrammetry and Remote Sensing,* **56**, 81-99, doi:10.1016/S0924-2716(01)00040-5.

Faruolo, M., T. Lacava, N. Pergola, and V. Tramutoli, 2018: On the potential of the RST-FLARE algorithm for gas flaring characterization from space. *Sensors,* **18**, 2466, doi:10.3390/s18082466.

Faruolo, M., I. Coviello, C. Filizzola, T. Lacava, N. Pergola, and V. Tramutoli, 2014: A satellite-based analysis of the Val d'Agri oil center (southern Italy) gas flaring emissions. *Nat.Hazards Earth Syst.Sci.,* **14**, 2783-2793, doi:10.5194/nhess-14-2783-2014.

Federation Council, 2019: Federation Council of the Federal Assembly of the Russian Federation,Accessed 7 August 2019, http://council.gov.ru/en/structure/regions/KHM/

Franklin, M., K. Chau, L. J. Cushing, and J. E. Johnston, 2019: Characterizing flaring from unconventional oil and gas operations in South Texas using satellite observations. *Environ.Sci.Technol.,* **53**, 2220-2228, doi:10.1021/acs.est.8b05355.

Friends of the Earth International, 2005: Gas Flaring in Nigeria: A Human Rights, Environmental, and Economic Monstrosity, Accessed 7 August 2019, https://www.foei.org/wp-content/uploads/2014/04/gasnigeria.pdf.

Gervet, B., 2007: "Gas Flaring Emission Contributes to Global Warming," Master's Thesis, Lule University of Technology, Lule.

Giglio, L., J. Descloitres, C. Justice, and Y. Kaufman, 2003: An enhanced contextual fire detection algorithm for MODIS. *Remote Sens.Environ.,* **87**, 273-282, doi:10.1016/S0034-4257(03)00184-6.

Giglio, L., J. D. Kendall, 2001: Application of the Dozier retrieval to wildfire characterization: a sensitivity analysis. *Remote Sens.Environ.,* **77**, 34-49.

Ismail, O., G. Umukoro, 2012: "Global Impact of Gas Flaring," Energy and Power Engineering, Vol. 4 No. 4, pp. 290-302. doi: 10.4236/epe.2012.44039.

Justice, C., L. Giglio, S. Korontzi, J. Owens, J. Morisette, D. Roy, J. Descloitres, S. Alleaume, F. Petitcolin, and Y. Kaufman, 2002: The MODIS fire products. *Remote Sens.Environ.,* **83**, 244-262, doi:10.1016/S0034-4257(02)00076-7.

Knizhnikov, A., Poussenkova, N., 2009: Russian associated gas utilization: Problems and Prospects, Annual Report within the Framework of the Project, Environment and Energy

LPDAAC, 2014: MOD14/MYD14 MODIS Terra/Aqua Thermal Anomalies V005, distributed by NASA EOSDIS Land Processes DAAC, Accessed 7 August 2019, https://lpdaac.usgs.gov/product_search

Matson, M., J. Dozier, 1981: Identification of subresolution high-temperature sources using a thermal IR sensor. *Photogramm.Eng.Remote Sensing*, **47**, 1311-1318.

Muirhead, K., A. Cracknell, 1984: Identification of gas flares in the North Sea using satellite data. *Int.J.Remote Sens.*, **5**, 199-212.

NCEI, 2019: NOAA JPSS Visible Infrared Imaging Radiometer Suite (VIIRS) Active Fires Environmental Data Record (EDR) from NDE. Data.nodc.noaa.gov, Accessed7August2019, https://data.nodc.noaa.gov/cgi-bin/iso?id=gov.noaa.ncdc:C00971

NGDC, 2019: VIIRS Nightfire V3.0, distributed by NOAA's National Geophysical Data Center, Accessed 7 August, 2019, https://ngdc.noaa.gov/eog/viirs/download_viirs_fire.html.

NGDC, 2014: VIIRS Nightfire V1.0, distributed by NOAA's National Geophysical Data Center, Accessed 7 August, 2019, https://ngdc.noaa.gov/eog/viirs/download_viirs_fire.html.

Nwanya, S. C., 2011: Climate change and energy implications of gas flaring for Nigeria. International Journal of Low Carbon Technologies, 6, 193-199.

Oil and Gas Eurasia, 2009: Flaring up - Companies pay high costs to be green, Accessed 15 July 2015, http://www.oilandgaseurasia.com/articles/p/97/article/883/

Peterson, D., J. Wang, C. Ichoku, E. Hyer, and V. Ambrosia, 2013: A sub-pixel-based calculation of fire radiative power from MODIS observations: 1: Algorithm

development and initial assessment. *Remote Sens.Environ.*, **129**, 262-279, doi:http://dx.doi.org/10.1016/j.rse.2012.10.036.

Polivka, T. N., E. J. Hyer, J. Wang, and D. A. Peterson, 2015: First global analysis of saturation artifacts in the VIIRS infrared channels and the effects of sample aggregation. *IEEE Geoscience and Remote Sensing Letters*, **12**, 1262-1266, doi:10.1109/LGRS.2015.2392098.

Rothery, D., M. Coltelli, D. Pirie, M. Wooster, and R. Wright, 2001: Documenting surface magmatic activity at Mount Etna using ATSR remote sensing. *Bull.Volcanol.*, **63**, 387-397.

Sharma, A., J. Wang, and E. M. Lennartson, 2017: Intercomparison of MODIS and VIIRS fire products in Khanty-Mansiysk Russia: Implications for characterizing gas flaring from space. *Atmosphere*, **8**, 95, doi:10.3390/atmos8060095.

Tramutoli, V., 2007: *Robust Satellite Techniques (RST) for natural and environmental hazards monitoring and mitigation: Theory and applications.* IEEE, 144 pp.

Weaver, J., D. Lindsey, D. Bikos, C. Schmidt, and E. Prins, 2004: Fire detection using GOES rapid scan imagery. *Weather and Forecasting*, **19**, 496-510, doi:10.1175/1520-0434(2004)019<0496:FDUGRS>2.0.CO;2.

World Bank, 2018: New satellite data reveals progress: Global gas flaring declined in 2017. Accessed 7 August 2019, https://www.worldbank.org/en/news/press-release/2018/07/17/new-satellite-data-reveals-progress-global-gas-flaring-declined-in-2017

World Bank, 2013: Igniting solutions to gas flaring in Russia, Accessed 11 March 2019, http://www.worldbank.org/en/news/feature/2013/11/12/igniting-solutions-to-gas-flaring-in-russia

Zhizhin, M., Elvidge, C. D., Hsu, F. C., & Baugh, K. E. 2013: Using the short-wave infrared for nocturnal detection of combustion sources in VIIRS data. *Proceedings of the Asia-Pacific Advanced Network, 35*, 49-61.